Extreme Nature of Four Blue-excess Dust-obscured Galaxies Revealed by Optical Spectroscopy

The Astrophysical Journal, 941:195 (15pp), 2022 December 20 https://doi.org/10.3847/1538-4357/aca403

Extreme Nature of Four Blue-excess Dust-obscured Galaxies Revealed by Optical Spectroscopy

Akatoki Noboriguchi[1,2,3], Tohru Nagao[4], Yoshiki Toba[5,6,7,4], Kohei Ichikawa[2], Masaru Kajisawa[3], Nanako Kato[3], Toshihiro Kawaguchi[8], Hideo Matsuhara[9,10], Yoshiki Matsuoka[4], Kyoko Onishi[11], Masafusa Onoue[12,13,14], Nozomu Tamada[3], Koki Terao[15,16], Yuichi Terashima[3,4], Yoshihiro Ueda[6], and Takuji Yamashita[5,4]

[1] School of General Education, Shinshu University, 3-1-1 Asahi, Matsumoto, Nagano 390-8621, Japan; akatoki@shinshu-u.ac.jp
[2] Frontier Research Institute for Interdisciplinary Sciences, Tohoku University, 6-3 Aramaki, Aoba-ku, Sendai, Miyagi 980-8578, Japan
[3] Graduate School of Science and Engineering, Ehime University, 2-5 Bunkyo-cho, Matsuyama, Ehime 790-8577, Japan
[4] Research Center for Space and Cosmic Evolution, Ehime University, 2-5 Bunkyo-cho, Matsuyama, Ehime 790-8577, Japan
[5] National Astronomical Observatory of Japan, 2-21-1 Osawa, Mitaka, Tokyo 181-8588, Japan
[6] Department of Astronomy, Kyoto University, Kitashirakawa-Oiwake-cho, Kyoto 606-8502, Japan
[7] Academia Sinica Institute of Astronomy and Astrophysics, 11F of Astronomy-Mathematics Building, AS/NTU, No.1, Section 4, Roosevelt Road, Taipei 10617, Taiwan
[8] Department of Economics, Management, and Information Science, Onomichi City University, Hisayamada 1600-2, Onomichi, Hiroshima 722-8506, Japan
[9] Institute of Space and Astronautical Science, Japan Aerospace Exploration Agency, 3-1-1 Yoshinodai, Chuo-ku, Sagamihara, Kanagawa 252-5210, Japan
[10] Department of Space and Astronautical Science, The Graduate University for Advanced Studies, SOKENDAI, 3-1-1 Yoshinodai, Chuo-ku, Sagamihara, Kanagawa 252-5210, Japan
[11] Department of Space, Earth and Environment, Chalmers University of Technology, Onsala Observatory, SE-439 92 Onsala, Sweden
[12] Kavli Institute for the Physics and Mathematics of the Universe (Kavli IPMU, WPI), The University of Tokyo, 5-1-5 Kashiwanoha, Kashiwa, Chiba 277-8583, Japan
[13] Kavli Institute for Astronomy and Astrophysics, Peking University, Beijing 100871, People's Republic of China
[14] Max-Planck-Institut für Astronomie, Königstuhl 17, D-69117, Heidelberg, Germany
[15] Subaru Telescope, National Astronomical Observatory of Japan, 650 North A'ohoku Place, Hilo, HI 96720, USA
[16] Astronomical Institute, Tohoku University, 6-3 Aramaki, Aoba-ku, Sendai, Miyagi 980-8578, Japan
Received 2022 January 17; revised 2022 November 10; accepted 2022 November 16; published 2022 December 23

Abstract

We report optical spectroscopic observations of four blue-excess dust-obscured galaxies (BluDOGs) identified by the Subaru Hyper Suprime-Cam. BluDOGs are a subclass of dust-obscured galaxies (DOGs; defined with the extremely red color $(i-[22])_{\rm AB} \geqslant 7.0$; Toba et al., showing a significant flux excess in the optical g and r bands over the power-law fits to the fluxes at the longer wavelengths. Noboriguchi et al. have suggested that BluDOGs may correspond to the blowing-out phase involved in a gas-rich major-merger scenario. However, the detailed properties of BluDOGs are not understood because of the lack of spectroscopic information. In this work, we carry out deep optical spectroscopic observations of four BluDOGs using Subaru/FOCAS and VLT/FORS2. The obtained spectra show broad emission lines with extremely large equivalent widths, and a blue wing in the C IV line profile. The redshifts are between 2.2 and 3.3. The averaged rest-frame equivalent widths of the C IV lines are 160 ± 33 Å, ~7 times higher than the average of a typical type 1 quasar. The FWHMs of their velocity profiles are between 1990 and 4470 km s^{-1}, and their asymmetric parameters are 0.05 and 0.25. Such strong C IV lines significantly affect the broadband magnitudes, which are partly the origin of the blue excess seen in the spectral energy distribution of BluDOGs. Their estimated supermassive black hole masses are $1.1 \times 10^8 < M_{\rm BH}/M_\odot < 5.5 \times 10^8$. The inferred Eddington ratios of the BluDOGs are higher than 1 ($1.1 < \lambda_{\rm Edd} < 3.8$), suggesting that the BluDOGs are in a rapidly evolving phase of supermassive black holes.

Unified Astronomy Thesaurus concepts: Active galaxies (17); Infrared galaxies (790); Galaxy evolution (594); Quasars (1319); Spectroscopy (1558)

1. Introduction

In the last two decades, observations of low-redshift galaxies have revealed tight correlations between the mass of supermassive black holes (SMBHs) and the host galaxy properties such as bulge mass (e.g., Magorrian et al. 1998; Gebhardt et al. 2000; Ferrarese & Merritt 2000; Tremaine et al. 2002; Marconi & Hunt 2003; Kormendy & Ho 2013; Ding et al. 2020). Such scaling relations suggest the so-called coevolution between galaxies and SMBHs. It has been argued that a major merger of gas-rich galaxies triggers active star-forming (SF) activity and subsequent mass accretion onto SMBHs (e.g., Sanders et al. 1988; Hopkins et al. 2008; Treister et al. 2012; Goulding et al. 2018). In this scenario, the two merging galaxies first evolve into a dusty SF galaxy. Then it evolves into a dusty active galactic nucleus (AGN) as gas accretion to the nuclear region triggers the activity of SMBHs. Finally, a dusty AGN evolves into an optically thin quasar after the surrounding dust is blown out by the powerful AGN outflow. The most active period of such SF and AGN activity is generally heavily obscured by dust, which prevents us from investigating these phases observationally.

By combining optical, near-infrared (NIR), and mid-infrared (MIR) catalogs obtained from the Subaru Hyper Suprime-Cam (HSC; Miyazaki et al. 2018)-Subaru Strategic Program (SSP; Aihara et al. 2018), the VISTA Kilo-degree Infrared Galaxy

Table 1
Photometric Data of BluDOGs

Name	HSC r Band (AB mag)	HSC i Band (AB mag)	WISE W3 Band (AB mag)	WISE W4 Band (AB mag)
HSC J090705.64+020955.8 (HSC J0907)	22.56 ± 0.01	22.59 ± 0.01	16.06 ± 0.13	14.89 ± 0.34
HSC J120200.84-011846.4 (HSC J1202)	20.92 ± 0.00	20.87 ± 0.00	14.47 ± 0.04	13.46 ± 0.10
HSC J120728.71-005808.4 (HSC J1207)	22.12 ± 0.01	22.31 ± 0.01	16.28 ± 0.16	15.01 ± 0.36
HSC J141435.21+003547.4	23.32 ± 0.02	23.11 ± 0.02	17.24[a]	15.33 ± 0.33
HSC J143727.40-011726.5	23.17 ± 0.02	23.10 ± 0.01	16.94 ± 0.23	15.37 ± 0.31
HSC J144333.84-000830.3 (HSC J1443)	22.34 ± 0.01	22.24 ± 0.01	16.14 ± 0.10	15.04 ± 0.23
HSC J144813.65+002244.3	23.55 ± 0.02	23.43 ± 0.02	16.83 ± 0.16	15.37 ± 0.34
HSC J144900.84+002350.2	23.95 ± 0.03	23.74 ± 0.02	17.15 ± 0.22	15.47 ± 0.36

Note.
[a] The magnitude is a 95% confidence upper limit. https://wise2.ipac.caltech.edu/docs/release/allwise/expsup/sec2_1a.html.

survey (VIKING; Arnaboldi et al. 2007), and the Wide-field Infrared Survey Explorer (WISE; Wright et al. 2010) all-sky survey (ALLWISE; Cutri 2014), Toba et al. (2015, 2017b) and Noboriguchi et al. (2019) selected dusty SF galaxies and/or powerful AGNs as dust-obscured galaxies (DOGs; Dey et al. 2008; Fiore et al. 2008; Bussmann et al. 2009, 2011; Desai et al. 2009). DOGs are defined with a very red optical–MIR color ($(i-[22])_{\rm AB} \geqslant 7.0$; Toba et al. 2015). DOGs represent a transition phase from a gas-rich major merger to an optically thin quasar in the gas-rich major-merger scenario (Dey et al. 2008), suggesting that some DOGs are expected to have buried AGNs. Recently, eight blue-excess DOGs (BluDOGs; Noboriguchi et al. 2019) were discovered from the HSC-selected DOGs based on their optical spectral slopes (i.e., $\alpha_{\rm opt} < 0.4$, where $\alpha_{\rm opt}$ is the observed-frame optical spectral index for the HSC g, r, i, z, and y bands in the power-law fit, $f_\nu \propto \lambda^{\alpha_{\rm opt}}$), and are a very rare population (eight BluDOGs out of 571 HSC-selected DOGs). Noboriguchi et al. (2019) suggested that BluDOGs with such blue excess may be in the blowing-out phase involved in the gas-rich major-merger scenario. However, the detailed properties of BluDOGs are not well understood because of the lack of spectroscopic information. Spectroscopic observations will give us accurate redshifts, and thus reliable AGN luminosities as a measure of the accretion rates, as well as the SMBH masses.

Another interesting population that may represent the transition phase between optically thick AGNs and optically thin quasars is extremely red quasars (ERQs; e.g., Ross et al. 2015; Hamann et al. 2017; Perrotta et al. 2019; Villar Martín et al. 2020). ERQs were identified by combining the optical photometric data of the Sloan Digital Sky Survey (SDSS; York et al. 2000), the optical spectroscopic data from SDSS-III (Eisenstein et al. 2011), the Baryon Oscillation Spectroscopic Survey (BOSS; Dawson et al. 2013), and the MIR photometric data of the WISE catalog. They are also defined with very red optical to MIR colors ($F_\nu(24\ \mu{\rm m})/F_\nu(R) \geqslant 1000$), and their spectra show broad emission lines with extremely large equivalent widths (EWs; Ross et al. 2015; Hamann et al. 2017). Hamann et al. (2017) refined the definition of ERQs as $(i-[12])_{\rm AB}>4.6$,[17] and reported notable blue-wing features in their C IV profiles, which suggests the presence of powerful outflow. However, the ERQ sample is limited to optically bright objects since their selection requires SDSS spectra. Detailed studies of optically faint populations in the transition phase between the optically thick and optically thin stages are required to understand the whole scenario of the merger-driven evolution of SMBHs. Therefore, it is important to execute the spectroscopic observations for BluDOGs and to research their spectroscopic properties.

In this work, we present the results of spectroscopic observations and subsequent analyses of four BluDOGs. This paper is organized as follows. We describe the sample selection of our targets and observations in Section 2. In Section 3, we present properties of the detected emission lines, the estimated dust extinctions, bolometric luminosities of an AGN ($L_{\rm bol}^{\rm AGN}$), and SMBH masses ($M_{\rm BH}$). A discussion of the large EWs of the C IV emission, their SMBH mass, and Eddington ratios is given in Section 4. Then we give a brief summary in Section 5. Throughout this paper, the adopted cosmology is a flat universe with $H_0 = 70\ {\rm km\ s^{-1}\ Mpc^{-1}}$, $\Omega_M = 0.3$, and $\Omega_\Lambda = 0.7$. Unless otherwise noted, all magnitudes refer to the AB system.

2. Sample and the Data

2.1. Sample Selection

In Noboriguchi et al. (2019), 571 DOGs were selected by combining $\sim$105 deg^2 imaging data obtained from the HSC-SSP[18] (g, r, i, z, and y), VIKING (Z, Y, J, H, and Ks), and ALLWISE (W1, W2, W3, and W4) surveys. The eight BluDOGs were defined among the DOG sample with the smallest observed-frame optical slope ($\alpha_{\rm opt} < 0.4$, where $\alpha_{\rm opt}$ is the observed-frame optical spectral index of the power-law fits to the HSC g-, r-, i-, z-, and y-band fluxes, $f_\nu \propto \lambda^{\alpha_{\rm opt}}$). We selected the four brightest BluDOGs ($r_{\rm AB} < 23$: see Table 1) as the targets of our spectroscopic observations presented in this paper.

2.2. Spectroscopic Observations and Data Reductions

We executed the observations by using Faint Object Camera and Spectrograph (FOCAS; Kashikawa et al. 2002) installed on

[17] All of the BluDOGs also satisfy the criterion of the ERQ (see Table 1).

[18] We utilize the photometric data of S16A HSC-SSP, which was released internally within the HSC survey team and is based on data obtained from 2014 March to 2016 April.

Table 2
Observation Log

Name	Exp. Time (s)	Date	Standard Star	Instrument
HSC J0907	900 × 2 600 × 1	2019 October 8	G191-B2B	FOCAS (Subaru)
HSC J1202	900 × 6	2019 February 27	LTT 6248	FORS2 (VLT)
HSC J1207	900 × 12	2019 March 1, 2, 6	LTT 4816	FORS2 (VLT)
HSC J1443	900 × 12	2019 March 7, 8	LTT 4816, EG 274	FORS2 (VLT)

Table 3
Detected Lines of J0907

Line Name (1)	$\lambda_{\rm rest}$ (Å) (2)	$z_{\rm line}$ (3)	FWHM$_{\rm rest}$ (Å) (4)	$F_{\rm line}$ (erg s^{-1} cm^{-2}) (5)	EW$_{\rm rest}$ (Å) (6)	$v_{\rm width}$ (km s^{-1}) (7)
C IV_R	1549.5	2.258 ± 0.001	12.8 ± 0.7	(1.10 ± 0.07)E−15	118 ± 10	2470 ± 130
C IV_B	1549.5	2.227 ± 0.004	13.8 ± 2.5	(2.87 ± 0.60)E−16	31.5 ± 6.7	2670 ± 490
C IV_R + C IV_B	1549.5	2.258 ± 0.002	15.2 ± 0.8	(1.39 ± 0.09)E−15	148 ± 12	2940 ± 150
He II_R	1640.4	2.260 ± 0.002	3.63 ± 2.32	(3.50 ± 2.36)E−17	4.43 ± 3.01	663 ± 425
He II_B	1640.4	2.235 ± 0.005	38.1 ± 5.9	(2.13 ± 0.48)E−16	26.8 ± 6.3	6960 ± 1080
He II_R + He II_B	1640.4	2.260 ± 0.002	5.54 ± 1.29	(2.48 ± 0.53)E−16	31.4 ± 7.0	1010 ± 240
O III]	1663.5	2.264 ± 0.001	3.29 ± 1.69	(4.49 ± 1.48)E−17	5.84 ± 1.98	593 ± 305
Si III	1892.0	2.258 ± 0.002	4.03 ± 4.16	(2.97 ± 2.55)E−17	3.56 ± 3.06	639 ± 659
C III]_R	1908.7	2.261 ± 0.005	30.3 ± 5.3	(2.34 ± 0.66)E−16	28.2 ± 8.1	4760 ± 830
C III]_R	1908.7	2.258 ± 0.002	6.19 ± 3.04	(6.50 ± 3.21)E−17	7.83 ± 3.89	971 ± 477
C III]_R + C III]_B	1908.7	2.258 ± 0.003	11.6 ± 1.7	(2.99 ± 0.73)E−16	36.0 ± 9.0	1830 ± 260
Mg II	2799.1	2.259 ± 0.001	17.6 ± 1.6	(2.44 ± 0.29)E−16	49.0 ± 7.3	1890 ± 170

Note. Column (1): line name, (2): rest-frame wavelength of the line, (3): line redshift, (4): rest-frame FWHM, (5): line flux, (6): REW, (7): velocity width after the correction for the instrumental broadening.

the Subaru Telescope of the National Astronomical Observatory of Japan, and FORS2 (Appenzeller et al. 1998) installed on the Very Large Telescope (VLT-UT1) of the European Southern Observatory (ESO). We present the observation log in Table 2.

2.2.1. Subaru FOCAS

By using FOCAS, we observed HSC J090705.64+020955.8 (hereafter J0907) on 2019 October 8, with an airmass of ∼1.76 and seeing of ∼0.″5. We used the 300B grism and the SY47 filter to cover $\lambda_{\rm obs} \sim 4700$–$9200$ Å, with the resultant spectral resolution of $R \sim 800$ for the 0.″8-width slit used. To reduce the obtained data, we performed bias correction, flat fielding with dome flat, removal of cosmic rays, spectral extraction, sky subtraction, wavelength calibration, and flux calibration with a standard star (G191-B2B) using the Python packages of `Astropy` and `NumPy`. For removing cosmic rays, we utilized `Astro-SCRAPPY` (McCully & Tewes 2019). `Astro-SCRAPPY` is based on the algorithm of `L.A.Cosmic`, which removes cosmic rays based on a variation of Laplacian edge detection (van Dokkum 2001). The final spectrum is an inverse-variance weighted mean of the individual shots, corrected for Galactic extinction (Schlegel et al. 1998).

2.2.2. VLT FORS2

By using FORS2, we observed HSC J120200.84-011846.4, HSC J120728.71-005808.4, and HSC J144333.84-000830.3 (hereafter, J1202, J1207, and J1443, respectively) between 2019 February 27 and March 8. We used the GRISM_600RI +19 and the GG435 filter to cover $\lambda_{\rm obs} \sim 5200$–$8000$ Å, which results in the spectral resolution of $R \sim 1500$ with a 0.″7 width slit. The typical airmasses of the observations for J1202, J1207, and J1443 were 1.17, 1.24, and 1.12, and the typical seeing sizes were ∼1.0, 0.5, and 0.″5, respectively. For the data reduction, we utilized the `Recipe flexible execution workbench` (`Reflex`; Freudling et al. 2013) software. `Reflex` performed bias correction, flat fielding with dome flat, sky subtraction, removing cosmic rays, spectral extraction, wavelength calibration, and flux calibration with a standard star (LTT 6248, LTT 4816, and EG 274). The final spectrum of each target is the inverse-variance weighted mean of the individual shots, corrected for Galactic extinction.

2.2.3. Spectrophotometric Recalibration

We recalibrated the reduced spectra to match the HSC photometry, in order to correct for the effects of the slit loss of the flux, systematic errors in the photometric and spectroscopic calibrations, and any other possible systematic errors. In our observations, the spectra cover the wavelength range of the HSC r band. We calculate the calibration factor, $f_{\rm photo\_calib} = F_{\rm photo\_}r/F_{\rm spec\_}r$, where $F_{\rm photo\_}r$ and $F_{\rm spec\_}r$ are the photometric and spectroscopic fluxes in the HSC r band. The derived calibration factors of J0907, J1202, J1207, and J1443 are 0.97, 1.50, 1.40, and 1.36, respectively. We multiplied the spectra with the derived calibration factors.

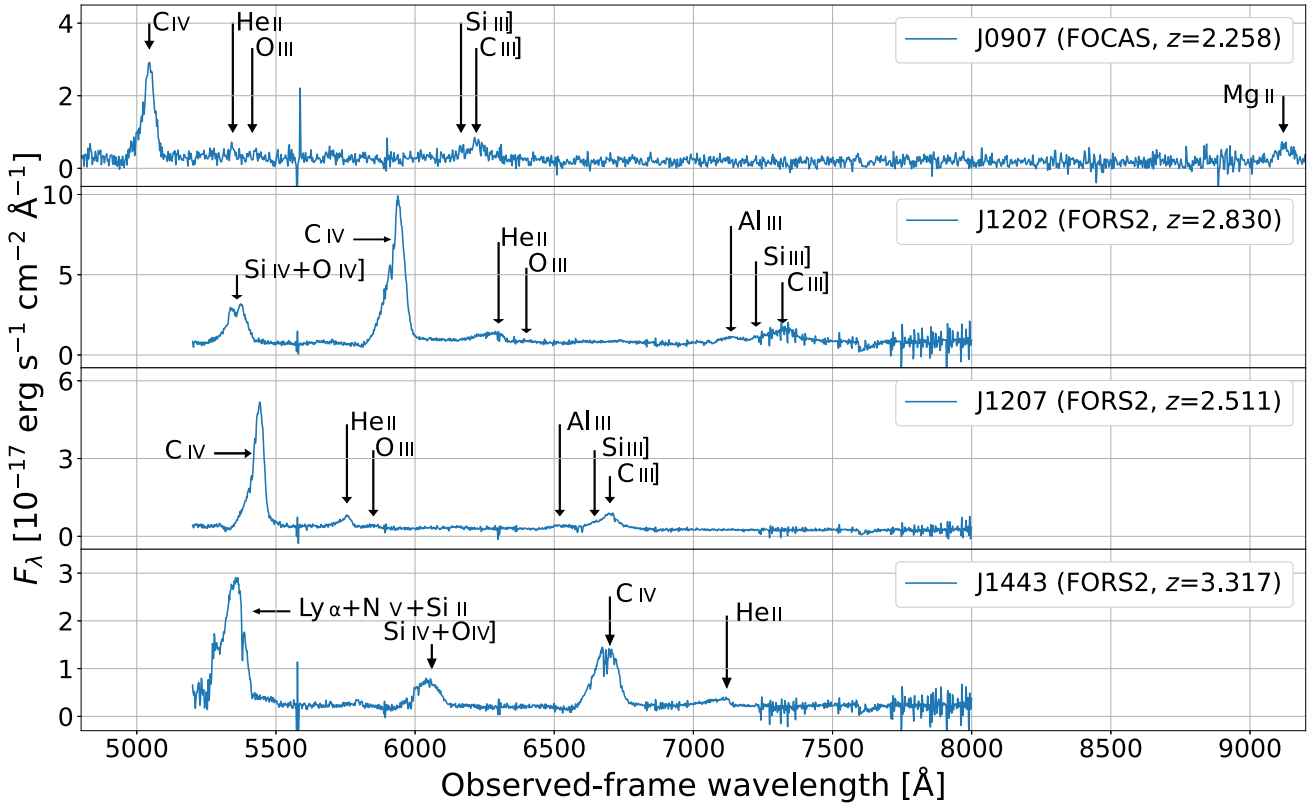

Figure 1. Reduced spectra of the BluDOGs. The spectra are for J0907, J1202, J1207, and J1443 from the top to bottom. Detected lines are marked by arrows and labels.

3. Results

3.1. Emission-line Measurements

Figure 1 shows the reduced spectra of the four BluDOGs. In order to measure the emission-line properties, we divide the emission lines into six groups as follows: (1) Lyα1216, N Vλ1240, and Si IIλ1263, (2) Si IVλ1397 and O IV]λ1402, (3) He IIλ1640 and O III]λ1663, and (4) Al IIIλ1857, Si III]λ1892, and C III]λ1909, (5) C IV 1549, and (6) Mg II. We fit the emission lines in each group simultaneously, with a linear continuum model subtracted from the observed spectrum. We adopt a single-Gaussian profile for Ly α, N V, Si II, Si IV, O IV], O III], Al III, Si III, and Mg II. The C III] of J1202 is fitted with a single-Gaussian profile, while those of J0907 and J1207 are fitted with a double-Gaussian profile. For the fit around the Si IV and O IV] of J1202, we added an additional Gaussian profile to reproduce the observed broad component. We fit C IV and He II with double-Gaussian profiles, and denote the blue and red components with the suffixes of "_B" and "_R," respectively. Additionally, we fit the doublet absorption lines observed around the C IV emission lines of J1202 and J1443. The C IV absorption lines observed at $\lambda_{\rm obs} = 5916.8$ and 5926.6 Å for J1202 and those at $\lambda_{\rm obs} = 6678.8$ and 6689.9 Å for J1443 are fitted using the Voigt profile, respectively. The doublet absorption line ratio is fixed as 2:1 (Feibelman 1983). The best values and standard deviations for emission and absorption lines parameters are estimated by using `scipy.optimize.curve_fit`,[19] while we calculate the FWHM of emission lines with a double Gaussian by using a Monte Carlo method. For this Monte Carlo simulation, we created 10,000 mock spectra using the noise arrays of the observed spectra, and calculated the mean and standard deviation of the line properties. The results for emission lines are listed in Tables 3–6. For the absorption lines, the observed-frame EWs and redshifts of the doublet absorption lines on the J1202 C IV emission line are 47.7 ± 19.6 Å, 23.6 ± 9.7 Å, and 2.822, respectively, while the observed-frame EWs and redshift of the doublet absorption lines on J1443 C IV emission line are 14.0 ± 6.3 Å, 6.94 ± 3.14 Å, and 3.314, respectively. Therefore, the comoving distance between J1202 and its C IV absorber is 8.73 Mpc, while that between J1443 and its C IV absorber is 2.79 Mpc.

The flux ratios of N V/Lyα and N V/C IV for J1443 are 3.9 and 1.8, respectively, whereas the values for the typical quasar (Vanden Berk et al. 2001) are 0.02 and 0.10. One possible reason for these unusual flux ratios in J1443 is the presence of absorption lines, which absorb most of the Lyα and the C IV fluxes around the peak. The unusual flux ratios cannot be explained by the dust reddening, given too small wavelength separations among the emission lines of Lyα, N V, and C IV.

Figure 2 shows the best-fit models to the C IV emission lines in the four BluDOGs. We adopt the C IV redshift taking C IV_R + C IV_B into account as the systemic redshift of the targets. The determined systemic redshifts of J0907, J1202, J1207, and J1443 are 2.258 ± 0.002, 2.830 ± 0.002, 2.511 ± 0.001, and 3.317 ± 0.006, respectively.

3.2. Emission-line Contributions to the HSC g- and r-band Magnitudes

Figure 1 suggests the very large EW of the emission lines. The average rest-frame EW (REW) of the C IV line of the four

[19] https://docs.scipy.org/doc/scipy/reference/

Table 4
Detected Lines of J1202

Line Name (1)	$\lambda_{\rm rest}$ (Å) (2)	$z_{\rm line}$ (3)	FWHM$_{\rm rest}$ (Å) (4)	$F_{\rm line}$ (erg s^{-1} cm^{-2}) (5)	EW$_{\rm rest}$ (Å) (6)	$v_{\rm width}$ (km s^{-1}) (7)
Si IV	1393.8	2.831 ± 0.001	4.27 ± 0.73	(1.56 ± 0.33)E−16	5.55 ± 1.17	919 ± 157
Broad component[a]	⋯	⋯	⋯	(1.23 ± 0.13)E−15	⋯	4970 ± 170
O IV]	1399.9	2.842 ± 0.001	9.90 ± 0.87	(5.13 ± 0.68)E−16	18.1 ± 2.4	2120 ± 190
C IV_R	1549.5	2.831 ± 0.001	15.0 ± 0.4	(5.46 ± 0.26)E−15	177 ± 9	2900 ± 70
C IV_B	1549.5	2.793 ± 0.002	13.0 ± 1.0	(7.98 ± 1.03)E−16	27.7 ± 3.6	2510 ± 190
C IV_R + C IV_B	1549.5	2.830 ± 0.002	16.0 ± 0.5	(6.26 ± 0.28)E−15	203 ± 10	3100 ± 90
He II_R	1640.4	2.838 ± 0.002	11.0 ± 1.7	(1.68 ± 0.47)E−16	5.06 ± 1.43	2010 ± 310
He II_B	1640.4	2.806 ± 0.005	21.1 ± 3.4	(3.16 ± 0.55)E−16	9.31 ± 1.64	3870 ± 620
He II_R + He II_B	1640.4	2.834 ± 0.004	25.5 ± 2.5	(4.84 ± 0.73)E−16	14.5 ± 2.2	4650 ± 450
O III]	1663.5	2.852 ± 0.003	7.57 ± 2.94	(2.06 ± 1.07)E−17	0.661 ± 0.343	1360 ± 530
Al III	1858.8	2.839 ± 0.002	21.5 ± 2.4	(3.05 ± 0.41)E−16	10.5 ± 1.4	3470 ± 390
Si III	1892.0	2.819 ± 0.004	13.6 ± 5.5	(9.40 ± 4.81)E−17	3.19 ± 1.64	2160 ± 870
C III]	1908.7	2.835 ± 0.002	30.6 ± 1.9	(1.01 ± 0.07)E−15	33.5 ± 2.4	4810 ± 300

Note. See Table 3 for the description of each column.
[a] The observed-frame wavelength, continuum flux, and FWHM of the broad component are 5349.5 ± 2.0 Å, (7.36 ± 0.12)E−18 erg s^{-1} cm^{-2} Å^{-1}, and 88.9 ± 2.9 Å, respectively. See Section 3.1 for details.

Table 5
Detected Lines of J1207

Line Name (1)	$\lambda_{\rm rest}$ (Å) (2)	$z_{\rm line}$ (3)	FWHM$_{\rm rest}$ (Å) (4)	$F_{\rm line}$ (erg s^{-1} cm^{-2}) (5)	EW$_{\rm rest}$ (Å) (6)	$v_{\rm width}$ (km s^{-1}) (7)
C IV_R	1549.5	2.512 ± 0.001	7.87 ± 0.43	(1.02 ± 0.08)E−15	74.2 ± 6.0	1520 ± 80
C IV_B	1549.5	2.500 ± 0.001	20.2 ± 0.5	(1.36 ± 0.09)E−15	99.3 ± 6.9	3900 ± 90
C IV_R + C IV_B	1549.5	2.511 ± 0.001	10.3 ± 0.4	(2.39 ± 0.12)E−15	173 ± 9	1990 ± 70
He II_R	1640.4	2.511 ± 0.001	6.53 ± 1.12	(6.61 ± 1.50)E−17	5.32 ± 1.21	1190 ± 210
He II_B	1640.4	2.499 ± 0.002	17.7 ± 1.3	(1.47 ± 0.24)E−16	11.7 ± 1.9	3240 ± 240
He II_R + He II_B	1640.4	2.509 ± 0.002	11.6 ± 1.2	(2.13 ± 0.28)E−16	17.2 ± 2.3	2120 ± 220
O III]	1663.5	2.516 ± 0.002	12.2 ± 2.4	(3.70 ± 0.95)E−17	3.18 ± 0.82	2200 ± 430
Al III	1858.8	2.508 ± 0.002	19.7 ± 1.7	(9.09 ± 1.02)E−17	9.23 ± 1.04	3180 ± 280
Si III	1892.0	2.511 ± 0.003	10.7 ± 4.9	(2.64 ± 1.60)E−17	2.79 ± 1.69	1690 ± 770
C III]_R	1908.7	2.510 ± 0.001	12.9 ± 1.4	(1.69 ± 0.25)E−16	18.2 ± 2.7	2030 ± 220
C III]_B	1908.7	2.503 ± 0.002	42.0 ± 2.9	(4.02 ± 0.65)E−16	43.1 ± 7.0	6600 ± 450
C III]_R + C III]_B	1908.7	2.509 ± 0.002	19.6 ± 1.2	(5.71 ± 0.70)E−16	61.4 ± 7.5	3080 ± 180

Note. See Table 3 for the description of each column.

Table 6
Detected Lines of J1443

Line Name (1)	$\lambda_{\rm rest}$ (Å) (2)	$z_{\rm line}$ (3)	FWHM$_{\rm rest}$ (Å) (4)	$F_{\rm line}$ (erg s^{-1} cm^{-2}) (5)	EW$_{\rm rest}$ (Å) (6)	$v_{\rm width}$ (km s^{-1}) (7)
Ly α	1215.7	3.341 ± 0.003	10.7 ± 2.6	(5.28 ± 1.31)E−16	64.3 ± 17.3	2650 ± 640
N V	1240.8	3.312 ± 0.001	16.8 ± 0.6	(2.06 ± 0.09)E−15	242 ± 23	4070 ± 160
Si II	1262.6	3.326 ± 0.003	16.0 ± 1.9	(1.24 ± 0.17)E−16	13.6 ± 2.0	3790 ± 450
Si IV	1393.8	3.324 ± 0.010	16.4 ± 3.2	(3.18 ± 1.01)E−16	33.8 ± 10.7	3520 ± 700
O IV]	1399.9	3.339 ± 0.008	12.9 ± 2.5	(1.74 ± 1.11)E−16	18.6 ± 11.8	2760 ± 540
C IV_R	1549.5	3.328 ± 0.005	14.2 ± 1.6	(6.15 ± 1.74)E−16	60.0 ± 17.0	2740 ± 310
C IV_B	1549.5	3.296 ± 0.007	15.7 ± 2.3	(5.47 ± 1.67)E−16	54.9 ± 16.8	3030 ± 440
C IV_R + C IV_B	1549.5	3.317 ± 0.006	23.1 ± 1.8	(1.16 ± 0.24)E−15	114 ± 24	4470 ± 350
He II_R	1640.4	3.337 ± 0.001	6.48 ± 1.56	(3.23 ± 1.01)E−17	3.24 ± 1.02	1180 ± 290
He II_B	1640.4	3.307 ± 0.004	20.3 ± 2.9	(9.15 ± 1.53)E−17	9.25 ± 1.56	3710 ± 530
He II_R + He II_B	1640.4	3.335 ± 0.003	20.1 ± 2.5	(1.24 ± 0.18)E−16	12.4 ± 1.9	3680 ± 460

Note. See Table 3 for the description of each column.

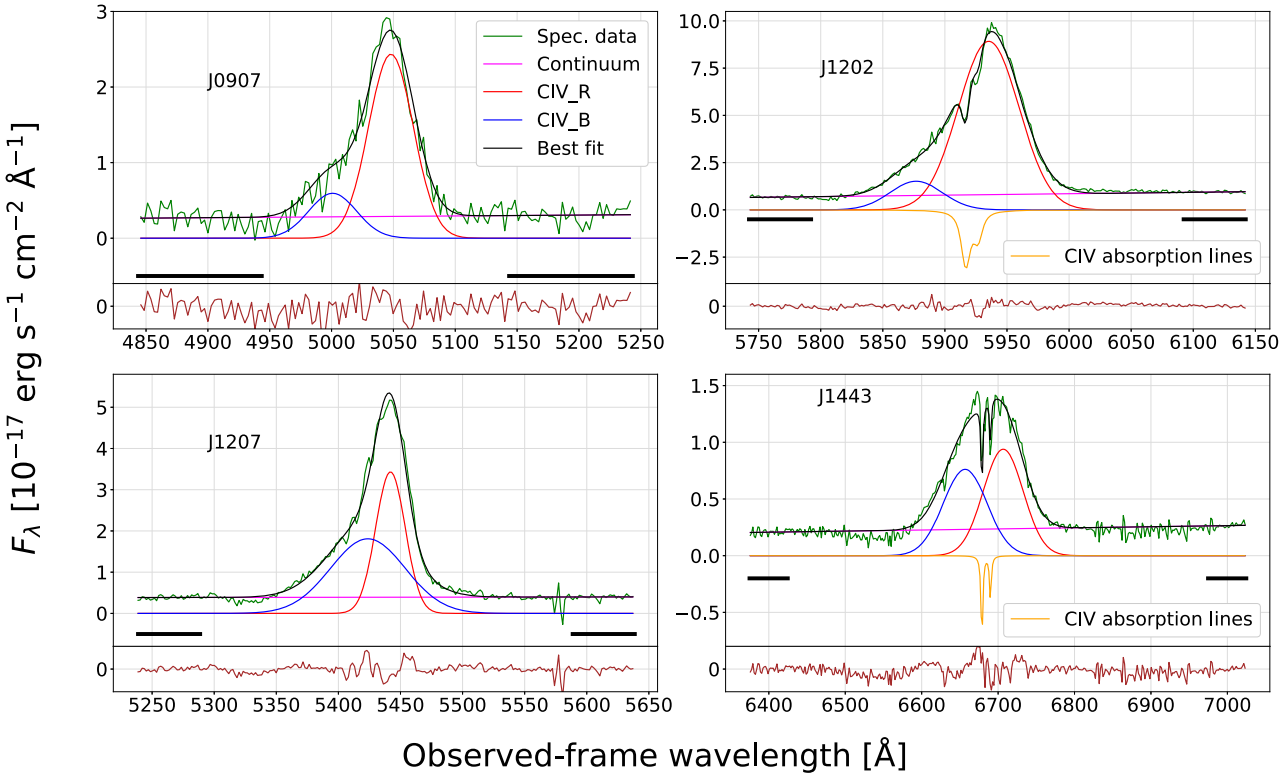

Figure 2. Spectral fits to the C IV emission lines of the BluDOGs. The top left, top right, bottom left, and bottom right panels show the C IV emission lines of J0907, J1202, J1207, and J1443, respectively. The green, magenta, red, blue, and black lines represent the observed spectrum, linear fit to the continuum emission, two Gaussians for the red and blue components, and best-fit model, respectively. The orange line in the J1202 and J1443 panels represents the C IV doublet absorption line. The horizontal black bars denote the wavelength range used to fit the continuum emission. In each panel, the lower part presents the residual of the best fit, with the same flux scale as in the upper part.

BluDOGs is 160 ± 33 Å, ~7 times higher than the average of SDSS type 1 quasars (23.8 ± 0.1 Å; Vanden Berk et al. 2001). Here, we investigate the effect of the large REWs on the HSC *g*- and *r*-band magnitudes.

First, we calculate the expected magnitudes at the *g* and *r* bands from an extrapolation of the power-law fit to the longer-wavelength bands (*i*, *z*, *y*, *Z*, *Y*, *J*, *H*, *Ks*, W1, W2, W3, and W4). Figure 3 clearly shows that the observed *g*- and *r*-band magnitudes exceed the extrapolation of the power-law fit. The excesses of the *g*-band magnitudes for J0907, J1202, J1207, and J1443 are 1.27, 1.13, 1.48, and 0.88 mag, and those for the *r*-band excesses are 0.47, 0.44, 0.65, and 0.40 mag, respectively.

Furthermore, we estimate the effect of the strong emission lines, based on their observed-frame EWs and the bandwidths (BWs) of the HSC *g* and *r* bands. The BWs of the HSC *g* and *r* bands are 1468 and 1508 Å (Kawanomoto et al. 2018), respectively. By taking all of the emission lines (Tables 3–6) covered by the HSC *g* band (4000–5500 Å) and *r* band (5500–7000 Å) into account, the total observed-frame EWs for J0907, J1202, J1207, and J1443 in the *g* band are 604, 258, 608, and 1380 Å, respectively, while those in the *r* band are 129, 836, 329, and 721 Å (Table 7). Note that the total observed-frame EWs in the *g* band are lower limits because our optical spectra do not cover the entire wavelength range of the band (Section 2.2) and thus some emission lines are not taken into account in the derived total observed-frame EWs. Especially Lyα, the strongest emission line in the rest-frame UV spectrum of typical AGNs, is not covered in our spectra of J0907, J1202, and J1207, thus, the total observed-frame EWs for these three objects are largely underestimated.[20] Since the magnitude excess by the emission lines is given by $\Delta\mathrm{mag} = 2.5\log(1 + \mathrm{EW}/\mathrm{BW})$, the estimated effects in the *g* band for J0907, J1202, J1207, and J1443 are 0.37, 0.18, 0.38, and 0.72 mag, respectively. Similarly, the estimated effects of emission lines to the *r*-band magnitudes are 0.09, 0.48, 0.21, and 0.42 mag, respectively (see Table 7 for a summary). We will discuss the implication of these estimates in Section 4.2.

3.3. Estimating the Dust Extinction

We need to estimate dust extinction, $E(B-V)$ of AGN radiation, and $L_{\mathrm{bol}}^{\mathrm{AGN}}$ to calculate the SMBH mass and Eddington ratio. Since Balmer decrement or other spectral measures of $E(B-V)$ are not available, we perform a spectral energy distribution (SED) fitting to the broadband photometry to estimate the $E(B-V)$ and $L_{\mathrm{bol}}^{\mathrm{AGN}}$. In this work, we utilize the new version of `Code Investigating GAlaxy Emission` (`CIGALE`; Burgarella et al. 2005; Noll et al. 2009; Boquien et al. 2019) called `X-CIGALE` (Yang et al. 2020), to perform the SED fit in a self-consistent framework by considering an energy balance between the UV/optical absorption and IR emission. `X-CIGALE` generates the best-fit model, including the stellar, AGN, and SF components that fit the photometric data in the rest-frame UV to far-infrared (FIR) bands. We utilize the Herschel Space Observatory (Pilbratt et al. 2010) Astrophysical Terahertz Large Area Survey (H-

[20] The Lyα line of J0907 is at the shorter edge of the HSC *g*-band coverage but the flux contribution to the *g*-band magnitude is likely to be significant owing to its broad nature.

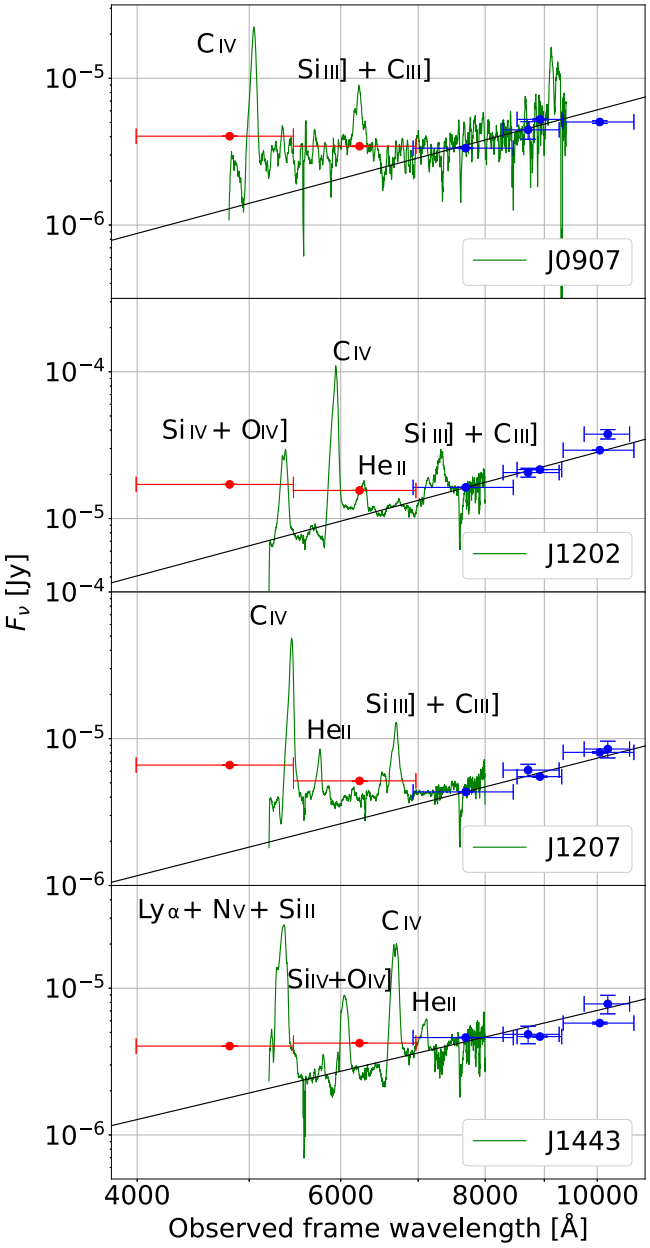

Figure 3. SED of J0907 (top), J1202 (middle upper), J1207 (middle lower), and J1443 (bottom). The red dots denote the *g*- and *r*-band magnitudes, while the blue dots denote the longer-wavelength optical and NIR magnitudes that are used for the power-law fit (black line). The green lines represent the observed spectra.

ATLAS; Eales et al. 2010; Bourne et al. 2016; Valiante et al. 2016) data observed with the Photodetector Array Camera and Spectrometer (PACS; Poglitsch et al. 2010) at 100 and 160 μm and with Spectral and Photometric Imaging REceiver (SPIRE; Griffin et al. 2010) at 250, 350, and 500 μm in the FIR, in addition to optical, NIR, and MIR data obtained by Subaru HSC, VISTA, and WISE. The 1σ limiting fluxes at 100, 160, 250, 350, and 500 μm are 44, 49, 7.4, 9.4, and 10.2 mJy, respectively (Valiante et al. 2016).

To search for the H-ATLAS counterpart of the four BluDOGs, we adopt a search radius of 10″ by following Toba et al. (2019) (and Toba et al. 2022). Accordingly, we found the counterparts of two BluDOGs (J1202 and J1207). The separation between the HSC position and the H-ATLAS

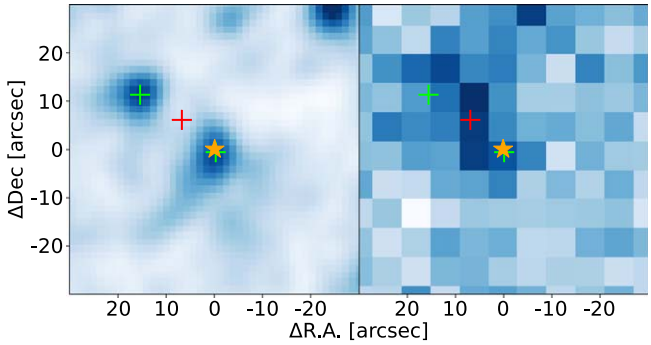

Figure 4. J1207 images in the WISE W1 band (left) and H-ATLAS 250 μm band (right). The orange stars, green crosses, and red cross denote source detections in the HSC-SSP, ALLWISE, and H-ATLAS catalogs, respectively. The size of each image is 60″ × 60″, centered at the HSC position of J1207.

counterpart position is 0.″94 for J1202, and 9.″7 for J1207. The relatively large separation in the latter case suggests the counterpart being a coincidental detection. There are two WISE sources around J1207 (Figure 4); one probably corresponds to J1207 itself (the angular separation between the HSC and WISE potions is 0.″65) and another is located 19″ away in the northeast direction. The H-ATLAS source is located between these two WISE sources, and thus the FIR fluxes given in the H-ATLAS catalog are possibly attributed to the two WISE sources. Therefore, we regard the H-ATLAS fluxes of J1207 as the upper limit. For the remaining two BluDOGs (J0907 and J1443), we adopt 5σ upper limit fluxes.

As for the optical–MIR photometric data, we utilize *g*, *r*, *i*, *z*, *y* (HSC-SSP), *Z*, *Y*, *J*, *H*, *Ks* (VIKING DR2), W1, W2, W3, and W4 (ALLWISE) bands (see Noboriguchi et al. 2019). Note that the signal-to-noise ratios (S/Ns) in these bands are more than 5, except for the W4 band with an S/N more than 3 because we adopted such an S/N cut in the selection of the DOGs (Noboriguchi et al. 2019). Since the *g*- and *r*-band photometries are significantly affected by the strong emission lines (see Figure 1 and Tables 3–6), which cannot be treated properly in `X-CIGALE`, we corrected for their contribution by referring to the estimates given in Table 7.

The models and parameters of `X-CIGALE` adopted in this work are summarized in Table 8. We assume a delayed star formation history (SFH; Ciesla et al. 2015) with the e-folding times of the main stellar population ($\tau_{\rm main}$) and late starburst population ($\tau_{\rm burst}$), mass fraction of the late burst population ($f_{\rm burst}$), and age of the main stellar population (age$_{\rm main}$) and the late burst (age$_{\rm burst}$). As the stellar population, we assume the initial mass function of Chabrier (2003), solar metallicity, and a 10 Gyr separation between young and old stellar populations (Age$_{\rm separation}$). The nebular emission model (Inoue 2011) is characterized by the ionization parameter (U), fractions of Lyman continuum photons escaping the galaxy ($f_{\rm esc}$) and absorbed by dust ($f_{\rm dust}$) and line width. We utilize a modified dust attenuation model presented by Boquien et al. (2019). The dust attenuation model for the continuum is taken from Calzetti et al. (2000) with the extension taken from Leitherer et al. (2002) between the Lyman break and 1500 Å. The emission lines are attenuated with a Milky Way extinction with $R_V = 3.1$ (Cardelli et al. 1989). We assumed $E(B-V)_{\rm continuum} = 0.44\ E(B-V)_{\rm line}$, following Calzetti et al. (2000). The $E(B-V)_{\rm line}$ is varied between 3 and 10. We utilize the `SKIRTOR` model as the AGN emission model, which takes the geometric parameters of the AGN into account and also allows us to

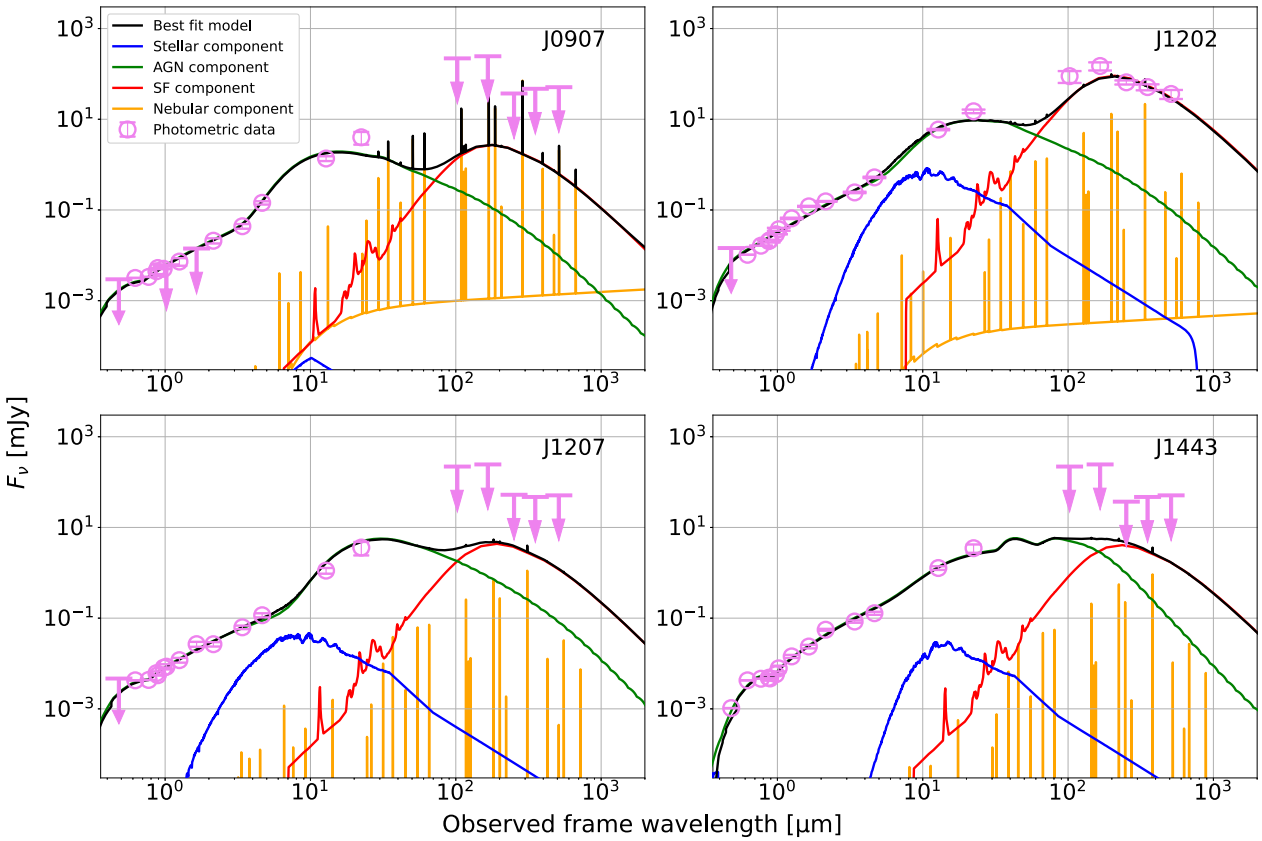

Figure 5. The results of the SED fitting for the four BluDOGs. The upper left, upper right, lower left, and lower right panels show the results of J0907, J1202, J1207, and J1443, respectively. The black, blue, green, red, and orange lines represent the best-fit model, stellar component (with dust attenuation), AGN component, SF component (FIR re-emission from the dust heated by SF), and nebular component, respectively. The magenta plots represent the photometric data. The arrows denote 5σ upper limit flux.

Table 7
Emission-line Contribution and Excess Magnitude to the Power-law Fit in the g and r Bands

	g Band			r Band		
	Total EWs (Å)	Δmag (AB mag)	Excess Mag (AB mag)	Total EWs (Å)	Δmag (AB mag)	Excess Mag (AB mag)
HSC J0907	>604	>0.37	1.27	129	0.09	0.47
HSC J1202	>258	>0.18	1.13	836	0.48	0.44
HSC J1207	>608	>0.38	1.48	329	0.21	0.65
HSC J1443	1380	0.72	0.88	721	0.43	0.40

Note. Δmag: $2.5\log(1 + \mathrm{EW/BW})$, Excess mag: the excesses of the g- and r-band magnitudes between the observed magnitudes and the expected magnitudes from an extrapolation of the power-law fit to the longer-wavelength bands.

incorporate the effect of extinction by the polar dust. The parameters of the AGN model are the average edge-on optical depth at 9.7 μm ($\tau_{9.7}$), the torus density parameters (p and q; Stalevski et al. 2016), the angle between the equatorial plane and the edge of the torus (oa), the ratio of the maximum to minimum radii of the dust torus (R_{ratio}), the fraction of total dust mass inside clumps (M_{cl}), the inclination (i), the AGN fraction (f_{AGN}), the extinction law, color excess ($E(B-V)^{\mathrm{AGN}}_{\mathrm{polar\ dust}}$), dust temperature ($T^{\mathrm{AGN}}_{\mathrm{polar\ dust}}$), and emissivity index of the polar dust.

The best-fit SED models are shown in Figure 5. The reduced χ^2 of the fits are 1.38, 3.19, 0.93, and 1.74 for J0907, J1202, J1207, and J1443, respectively. The best-fit values and associated errors for $E(B-V)^{\mathrm{AGN}}_{\mathrm{polar\ dust}}$ and $L^{\mathrm{AGN}}_{\mathrm{bol}}$ are estimated with the Bayesian-like strategy presented in Noll et al. (2009), and are reported in Table 9. On the other hand, we cannot quantitatively constrain the parameters of the host galaxies because the $E(B-V)$ values are too large and the optical parts in their SEDs are dominated by their AGN emission (see Figure 5).

3.4. Measurement of the SMBH Mass

We have detected the C IV emission line for all four BluDOGs and the Mg II emission line for J0907, both of which are widely used to calculate the SMBH mass of type 1 AGNs. Note that the systematic uncertainty is larger in the C IV-based SMBH mass than in the Mg II-based SMBH mass, due to a powerful outflow sometimes seen in the C IV velocity profile (e.g., Baskin & Laor 2005; Netzer 2015; Coatman et al. 2017). We calculate the single-epoch mass of SMBHs with the C IV

Table 8
Parameters Adopted in the X-CIGALE Fit

Parameter	Value
Delayed SFH (Ciesla et al. 2015)	
$\tau_{\rm main}$ [Myr]	100, 250, 500
$\tau_{\rm burst}$ [Myr]	10, 50
$f_{\rm burst}$	0.0, 0.5, 0.99
Age$_{\rm main}$ [Myr]	500, 800, 1000
Age$_{\rm burst}$ [Myr]	1, 5, 10
Single Stellar Population (Bruzual & Charlot 2003)	
IMF	Chabrier (2003)
Metallicity	0.02
Age$_{\rm separation}$ [Myr]	10
Nebular Emission (Inoue 2011)	
$\log U$	−2.0
$f_{\rm esc}$	0.0
$f_{\rm dust}$	0.0
Line width [km s^{-1}]	300.0
Dust Attenuation (Calzetti et al. 2000)	
$E(B-V)_{\rm line}$	3, 4, 5, 6, 7, 8, 9, 10
$f_{E(B-V)}$	0.44
$\lambda_{\rm UV,\ bump}$ [nm]	217.5
FWHM$_{\rm UV,\ bump}$ [nm]	35.0
$A_{\rm UV,\ bump}$	0.0
δ	0.0
Extinction law of emission lines	the Milky Way
R_V	3.1
Dust Emission (Dale et al. 2014)	
AGN fraction	0.0
$\alpha_{\rm IR,\ AGN}$	0.0625, 0.2500, 2.0000
AGN Model (Stalevski et al. 2016)	
$\tau_{9.7}$	3, 7
p	1.0
q	1.0
oa [deg]	10, 20, 30, 40, 50, 60, 70, 80
$R_{\rm ratio}$	20
$M_{\rm cl}$	0.97
i [deg]	0, 10, 20, 30, 40, 50, 60, 70, 80, 90
$f_{\rm AGN}$	0.1, 0.3, 0.5, 0.7, 0.9
Extinction law of polar dust	Calzetti et al. (2000)
$E(B-V)^{\rm AGN}_{\rm polar\ dust}$	0.1, 0.2, 0.3, 0.4, 0.5
$T^{\rm AGN}_{\rm polar\ dust}$ [K]	600, 700, 800, 900, 1000, 1100, 1200, 1300, 1400
Emissivity of polar dust	1.6

and Mg II emission lines, following the calibrations given in Vestergaard & Peterson (2006) and Vestergaard & Osmer (2009), respectively:

$$M_{\rm BH} = 10^{6.66}\left(\frac{\rm FWHM(C\ IV)}{10^3\ \rm km\ s^{-1}}\right)^2\left(\frac{\lambda L_\lambda(1350\text{Å})}{10^{44}\ \rm erg\ s^{-1}}\right)^{0.53} M_\odot, \quad (1)$$

and

$$M_{\rm BH} = 10^{6.86}\left(\frac{\rm FWHM(Mg\ II)}{10^3\ \rm km\ s^{-1}}\right)^2\left(\frac{\lambda L_\lambda(3000\text{Å})}{10^{44}\ \rm erg\ s^{-1}}\right)^{0.5} M_\odot, \quad (2)$$

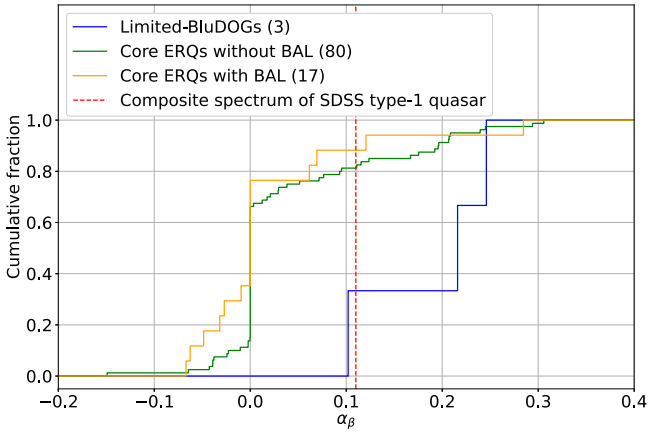

Figure 6. Cumulative distribution of the α_β indices for the limited BluDOGs (see the main text; blue line), core ERQs without BALs (green line), and core ERQs with BALs (orange line). The red-dashed line denotes the α_β index measured for the composite spectrum of SDSS type 1 quasars.

where FWHM(C IV), FWHM(Mg II), λL_λ(1350Å), and λL_λ(3000Å) are the FWHM of the C IV and Mg II velocity profile, and the monochromatic luminosity at 1350 and 3000 Å, respectively. Note that we use the FWHM of C IV_R + C IV_B as the FWHM of the C IV. We cannot eliminate the possibility that the estimated SMBH masses are overestimated because the C IV profiles are affected by nucleus outflows (Section 4.1). For estimating the reddening-corrected monochromatic luminosity, we use the optical spectra presented in Section 3.1. We converted the spectra to the rest-frame, dereddened them with $E(B-V)^{\rm AGN}_{\rm polar\ dust}$ derived in the SED fit, and masked out emission and absorption lines as well as pixels with negative values. Then, we fit a power-law continuum model to the spectra and estimate the monochromatic luminosities from the best fits. The estimated λL_λ(1350) of J0907, J1202, J1207, and J1443 are $(1.54\pm0.05)\times10^{45}$, $(9.64\pm0.27)\times10^{45}$, $(3.06\pm0.06)\times10^{45}$, and $(2.93\pm0.03)\times10^{45}$ erg s^{-1}, respectively. The λL_λ(3000) of J0907 is estimated to be $(1.45\pm0.04)\times10^{45}$ erg s^{-1}.

The resultant SMBH masses are summarized in Table 9. It should be noted that the C IV-based $M_{\rm BH}$ and Mg II-based $M_{\rm BH}$ of J0907 is not consistent within the statistical error. This is probably attributable to a systematic error, especially in the C IV-based $M_{\rm BH}$, known to be accompanied by a large systematic error (∼0.5 dex; see, e.g., Shen 2013). Hereafter, we use only the C IV-based $M_{\rm BH}$, since it is measured in all the four BluDOGs.

4. Discussion

4.1. Spectral Features and Nuclear Outflows

We found that the redshifts of the four BluDOGs are in the range of $2.2 \lesssim z_{\rm sp} \lesssim 3.3$. They are systematically higher than the typical redshifts of DOGs ($z_{\rm sp} = 1.99 \pm 0.45$; Dey et al. 2008; Pope et al. 2008). One possible reason for this systematically high redshift is a selection effect related to the blue-excess criterion. When we select BluDOGs from the parent DOG sample, the g- and r-band magnitudes show an excess of the expected magnitudes estimated by the power-law extrapolation from the i band to the W4 band. Thus, we may select DOGs in a preferred redshift range where strong emission lines such as Lyα and C IV shift into the two bands

Table 9
Physical Properties of the Four BluDOGs

	HSC J0907	HSC J1202	HSC J1207	HSC J1443
Redshift	2.258 ± 0.002	2.830 ± 0.002	2.511 ± 0.001	3.317 ± 0.006
$E(B-V)^{\rm AGN}_{\rm polar\ dust}$	0.26 ± 0.05	0.33 ± 0.04	0.30 ± 0.02	0.20 ± 0.01
$L^{\rm AGN}_{\rm bol}/L_\odot$	$(6.11 \pm 0.95) \times 10^{12}$	$(6.11 \pm 1.18) \times 10^{13}$	$(7.95 \pm 1.47) \times 10^{12}$	$(2.52 \pm 0.13) \times 10^{13}$
$M_{\rm BH}$ (C IV)$/M_\odot$	$(1.69 \pm 0.17) \times 10^{8}$	$(4.95 \pm 0.30) \times 10^{8}$	$(1.11 \pm 0.08) \times 10^{8}$	$(5.48 \pm 0.86) \times 10^{8}$
$M_{\rm BH}$ (Mg II)$/M_\odot$	$(9.85 \pm 1.80) \times 10^{7}$	…	…	…
$\lambda_{\rm Edd}$ (C IV)	1.10 ± 0.20	3.75 ± 0.76	2.19 ± 0.43	1.40 ± 0.23

(see Section 4.2 for more quantitative assessments). The reason for the underestimated photometric redshift ($\sim$1; Noboriguchi et al. 2019) is the unusual emission lines with the large REW.

The detected emission lines have large velocity widths, $\gtrsim$2000 km s^{-1} in most cases. This suggests that the broad-line region (BLR) of the BluDOGs is not completely obscured; in other words, the observed BluDOGs are classified as type 1 AGNs. This is an unexpected result because their very red color between optical and MIR suggests the heavily obscured nature. One possible interpretation is that we are looking at a phase where the surrounding dust is just blown away by the nuclear activity (outflow, radiation pressure, or both), as discussed further in Section 4.3. It should be noted that the type 1 nature is seen not only in the presented BluDOGs but also in some other DOGs (e.g., Toba & Nagao 2016; Toba et al. 2017a; Zou et al. 2020). Systematic spectroscopic observations for the whole population of DOGs are required to study the nature of obscuration occurring in various populations of DOGs.

As shown in Figure 2, the velocity profile of the observed C IV lines shows a notable excess feature in the blue wing. Such an excess in the C IV velocity profile has been observed in other type 1 AGNs and interpreted as a result of powerful nuclear outflows (e.g., Baskin & Laor 2005; Netzer 2015; Coatman et al. 2017). To evaluate quantitatively how the nuclear outflow in BluDOGs is strong compared to ordinary AGNs, we examine the *asymmetry parameter* (α_β) defined by De Robertis (1985) as

$$\alpha_\beta = \frac{\lambda_c(3/4) - \lambda_c(1/4)}{\Delta\lambda(1/2)}, \quad (3)$$

where $\lambda_c(h)$ and $\Delta\lambda(1/2)$ are the central wavelengths at which the flux falls to the h time of the peak flux and FWHM of the broad profile, respectively. The positive and negative values of α_β express the blue and red excesses, respectively. The derived values of α_β for J0907, J1202, J1207, and J1443 are 0.216, 0.102, 0.246, and 0.051, respectively. As a reference, the C IV velocity profile in the composite spectrum of SDSS type 1 quasars given by Vanden Berk et al. (2001) shows $\alpha_\beta = 0.110$. Thus, J0907 and J1207 may possess a significant nuclear outflow that is more powerful than typical quasars.

In order to compare α_β of the BluDOG with that of another dusty AGN population, we fitted the C IV profile of 97 *core* ERQs (ERQs with REW(C IV) >100 Å) in Hamann et al. (2017) and measured α_β by adopting a single or double-Gaussian profile. The core ERQ sample consists of 80 objects without broad absorption lines (BALs) and 17 objects with BALs, and we investigate the statistics of α_β for the two subsamples separately because the BAL feature can affect the C IV line profile. Here, we exclude J1443 from the BluDOG sample when comparing the α_β index because its velocity profile is largely affected by narrow absorption lines (hereafter the limited-BluDOG sample to infer the three BluDOGs; i.e., J0907, J1202, and J1207). Figure 6 shows the cumulative fraction of α_β for the limited BluDOGs, core ERQs without BALs, and core ERQs with BALs. The averaged values of the limited BluDOGs, core ERQs without BALs, and core ERQs with BALs are 0.15 ± 0.08, 0.02 ± 0.13, and 0.01 ± 0.09, respectively. We performed the Kolmogorov–Smirnov test (K-S test) to examine the statistical significance of the difference in α_β among the samples. The p-values of the limited-BluDOG-core ERQs without BALs, and limited-BluDOG-core ERQs with BALs are 0.0178 and 0.0175, respectively. Thus, we conclude that the distributions of α_β of the limited BluDOGs and core ERQs with/without BALs are marginally different with $>2\sigma$ significance. This suggests that the BluDOGs show a nuclear outflow that is possibly more powerful than the nuclear outflow in core ERQs with/without BALs.

We also focus on the kurtosis index (kt_{80}) defined as follows (see Hamann et al. 2017 for details): $kt_{80} = \Delta v(80\%)\ /\Delta v(20\%)$, where $\Delta v(x\%)$ is the velocity width at $x\%$ of the peak flux height. In addition to α_β, this kt_{80} index is useful to characterize the C IV wing (a more prominent blue wing results in a smaller kt_{80}). By using the best-fit double-Gaussian profile of the BluDOGs, kt_{80} of J0907, J1202, J1207, and J1443 are 0.276, 0.313, 0.252, and 0.440, respectively. Again we exclude J1443 from the BluDOG sample when comparing the kt_{80} index with the discussion of the α_β index. For comparison, the kt_{80} of a single Gaussian is $\sqrt{1 - \frac{2\ln(2)}{\ln(5)}}$ ($\sim$0.37), whereas most quasars have $kt_{80} \sim 0.15$–0.30 (see Figure 7 in Hamann et al. 2017). The limited BluDOGs, core ERQs without BALs, and core ERQs with BALs show $kt_{80} = 0.28 \pm 0.03$, 0.33 ± 0.06, and 0.34 ± 0.05, respectively (see also Figure 7). Note that the C IV profile of the 41 core ERQs without BALs and seven core ERQs with BALs is fitted by a single Gaussian, which is the reason why many objects have $kt_{80} \sim 0.37$ as shown in Figure 7. The C IV velocity profiles of core ERQs with/without BALs are roughly consistent with the Gaussian without a blue wing. However, the kt_{80} index of the limited BluDOGs is less than $\sqrt{1 - \frac{2\ln(2)}{\ln(5)}}$, suggesting that their C IV line profile has a wing. We performed the K-S test to examine the statistical significance of the difference in kt_{80} among the samples. The p-values of the limited-BluDOGs-core ERQs without BALs, and limited-BluDOGs-core ERQs with BALs are 0.0637 and 0.0175, respectively. Therefore, we conclude that the distributions of kt_{80} between the samples of the limited BluDOGs and core ERQs with/without the BAL feature are marginally different with $>2\sigma$ significance.

It has been reported that AGNs with a high Eddington ratio tend to show a Lorentzian-line velocity profile in BLR lines (e.g., Moran et al. 1996; Véron-Cetty et al. 2001; Collin et al. 2006;

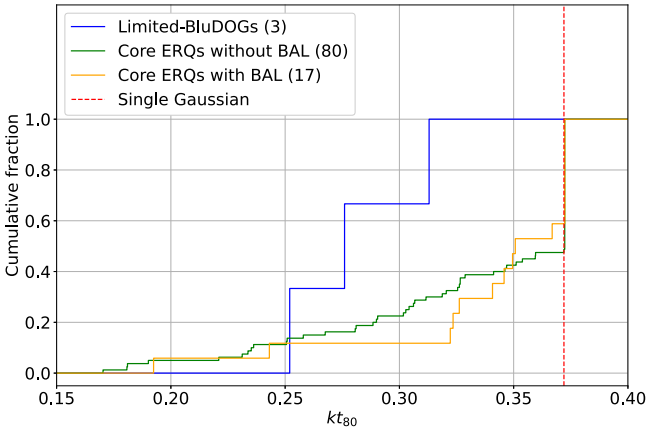

Figure 7. Cumulative distribution of the kt_{80} indices for the limited BluDOGs (blue line), core ERQs without BALs (green line), and core ERQs with BALs (orange line). The red-dashed line denotes the kt_{80} index for the single-Gaussian profile.

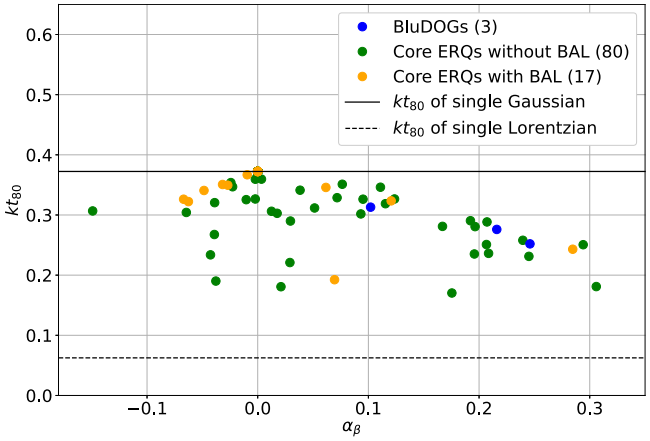

Figure 8. kt_{80} vs. α_β plot for the limited BluDOGs (blue dots), core ERQs without BALs (green dots), and core ERQs with BALs (orange dots). The black solid line and dashed line denote the kt_{80} values of a single Gaussian and single Lorentzian, respectively. Note that 41 core ERQs without BALs and seven core ERQs with BALs are fitted with a single Gaussian, and they are plotted at $(\alpha_\beta, kt_{80}) = (0, \sqrt{1-\frac{2\ln(2)}{\ln(5)}})$.

Zamfir et al. 2010). Therefore, the small kt_{80} value of BluDOGs can be caused by the contribution of extended Lorentzian wings instead of the asymmetric blue wing. For a symmetric Lorentzian profile, $kt_{80} \sim 1/16$ (much smaller than a Gaussian profile, $kt_{80} \sim 0.37$) and $\alpha_\beta = 0$ are expected. However, the BluDOGs are inconsistent with this expectation (Figure 8). Figure 8 also shows that the BluDOGs follow the trend made by core ERQs with/without BALs in the kt_{80}–α_β plane, while a systematic deviation of BluDOGs toward $(\alpha_\beta, kt_{80}) = (0, 0)$ is expected if a Lorentzian component significantly contributes to the C IV line of BluDOGs. Thus, we conclude that extended Lorentzian wings do not affect the C IV line profile of BluDOGs, but the small kt_{80} of BluDOGs is caused by the asymmetric blue excess due to the stronger nuclear outflow than that of ERQs.

4.2. Large EWs of the C IV Emission

As we summarized in Table 7, the blue excess in J1443 can almost be explained by the contribution of the strong emission lines. This is also the case for J1202 by taking into account the additional contribution of unobserved Lyα to the g band. On the other hand, the blue excess of the remaining two BluDOGs cannot be explained only by the contribution of BLR emission lines. Figure 3 strongly suggests that a part of the excess flux comes from the continuum emission, which deviates at $\lesssim$7000 Å from the extrapolation of the power-law fit. These results demonstrate the complexity and diversity of BluDOGs; systematic exploration of a larger sample is required to statistically understand the origin of the blue excess.

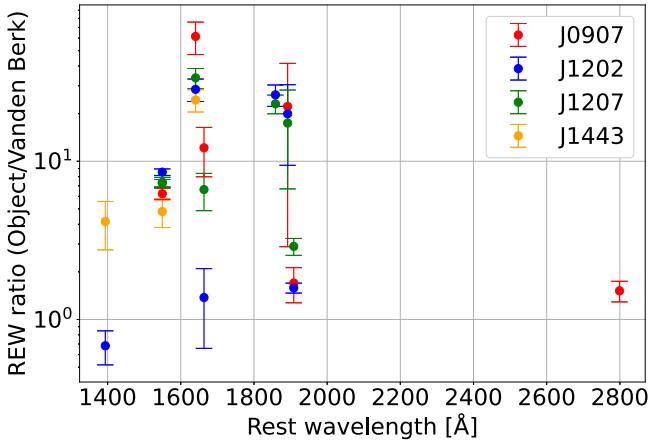

Figure 9. REW ratio vs. rest-frame wavelength. REW ratios are defined as REWs of objects over REWs from the composite spectrum of SDSS type 1 quasar measured by Vanden Berk et al. (2001). The red, blue, green, and orange plots show the REW ratios of J0907, J1202, J1207, and J1443, respectively.

Not only REW(C IV), but the REW of other BLR emission lines are also systematically larger than observed in typical type 1 quasars (see Tables 3–6, Figure 9, and also Table 2 in Vanden Berk et al. 2001). Such a trend may be explained if the observed BluDOGs have lower UV luminosity than typical quasars owing to the Baldwin effect (Baldwin 1977; Kinney et al. 1990; Baskin & Laor 2004), i.e., the negative correlation between the REWs and the continuum luminosities of quasars. Figure 10 shows the four BluDOGs in the C IV REW versus λL_λ(1350 Å) diagram. Note that the REW of J1443 (114 ± 24 Å) is somewhat smaller than that of the remaining three BluDOGs (148 ± 12, 203 ± 10 and 173 ± 9 Å for J0907, J1202, and J1207, respectively; see Tables 3–6). This is partly because of an underestimation of the C IV flux caused by the absorption features. The figure also shows SDSS type 1 quasars with reliable measurement of C IV REW (`EWCIV/e_EWCIV > 5`) and without BALs (`BAL < 1`) taken from Shen et al. (2011). Since the Baldwin effect does not significantly depend on redshift (e.g., Dietrich et al. 2002; Croom et al. 2002; Niida et al. 2016), we do not adopt any redshift criterion to select the SDSS quasars so that a wide luminosity range is covered. We also use another comparison sample taken from the WISE/SDSS selected hyper-luminous quasar sample (WISSH; Bischetti et al. 2017; Vietri et al. 2018),[21] in order to add objects at the high-luminosity end.

Figure 10 clearly shows that the C IV REWs of BluDOGs are larger than the comparison samples at a given UV luminosity.

[21] The C IV REW and C IV line luminosity of WISSH quasars are given by Vietri et al. (2018). To calculate L_λ(1350 Å) of WISSH quasars, we assume that the continuum spectrum of WISSH quasars is a power law and adopt the following formula: $L_\lambda(1350\text{Å}) = \frac{L^{\rm line}(\text{C IV})}{\text{REW(C IV)}} \times \left(\frac{1350}{1549}\right)^{\alpha_\lambda}$, where L_λ(1350Å), $L^{\rm line}$(C IV), and α_λ are the monochromatic luminosity at 1350 Å, the line luminosity of C IV, and power-law index, respectively. Here, we adopt $\alpha_\lambda = -1.7$ (Vanden Berk et al. 2001) as the power-law index.

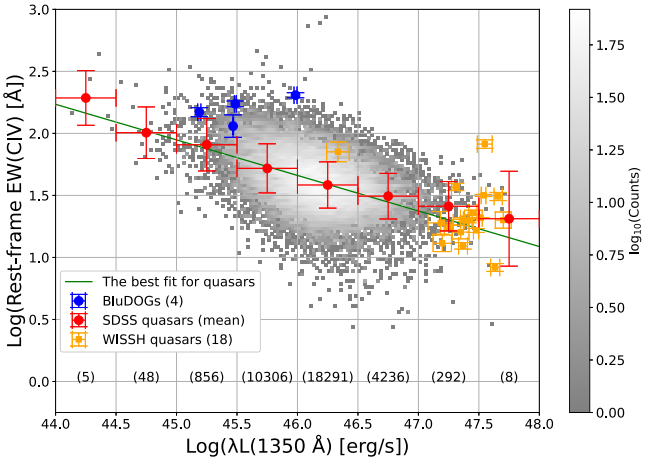

Figure 10. REW of the C IV vs. the monochromatic luminosity at 1350 Å. Blue and orange dots represent the four BluDOGs and WISSH quasars (Vietri et al. 2018). The gray 2D histogram represents the number density of the SDSS quasars (Shen et al. 2011). The green line represents the linear fit to the distribution of the SDSS quasars. The red plots show the mean and standard deviation in luminosity bins with 0.5 dex width. The numbers of SDSS quasars in the individual bins are shown at the bottom of the panel.

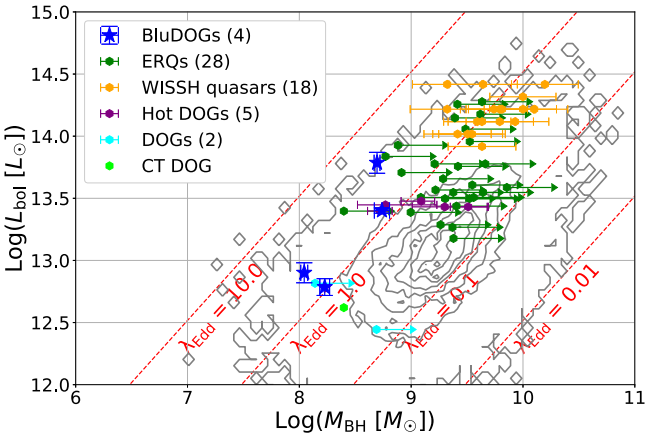

Figure 11. Diagram of SMBH mass vs. bolometric luminosity. The filled-blue stars and gray contour denote the BluDOGs and SDSS quasars, while the filled hexagons with green, orange, purple, cyan, and light green colors denote ERQs (Perrotta et al. 2019), WISSH quasars (Vietri et al. 2018), Hot DOGs (Wu et al. 2018), DOGs (Melbourne et al. 2011, 2012), and a CT DOG (Toba et al. 2020), respectively. The red-dashed lines represent a constant Eddington ratio of $\lambda_{\rm Edd} = 0.01$, 0.1, 1.0, and 10.0.

The excess REW over the average relation of the Baldwin effect (shown with a green solid line in Figure 10) for J0907, J1202, J1207, and J1443 are 0.29, 0.66, 0.44, and 0.26 dex, respectively. This excess is larger than the scatter of the comparison samples (see red plots in Figure 10). Therefore, the large REW seen in the BluDOGs is not due to the Baldwin effect.

The averages and standard deviations of REW(C IV) for core ERQs and ERQ-like objects are 178 ± 74 and 86 ± 45 Å, respectively (Hamann et al. 2017). The distributions of REW (C IV) and $(i - {\rm W3})_{\rm AB}$ color for BluDOGs are consistent with these of core ERQs, although most core ERQs and ERQ-like objects do not show a blue-wing profile in C IV (Section 4.1). Hamann et al. (2017) proposed a scenario in which the large REW of ERQs is possibly due to the spatially extended geometry of BLRs caused by the powerful nuclear outflow. If the obscuration is heavier for the accretion disk than for the BLRs, which have extended geometry, the continuum emission is more heavily extinct than the BLR emission lines and thus the observed-frame EW becomes larger. Such a scenario may also apply to BluDOGs. Unfortunately, it is not observationally feasible to confirm this idea by resolving the spatial structure of BLRs in ERQs or BluDOGs due to the required angular resolution, even with JWST or existing ground-based interferometers. Without spatially resolving them, a possible approach is the velocity-resolved reverberation mapping of the geometry and kinematics of BLR clouds (e.g., Horne et al. 2004; Denney et al. 2009; Li et al. 2013; Kollatschny et al. 2014; Pancoast et al. 2014).

4.3. Possible Extreme Accretion and the Nature of BluDOGs

To understand the nature of BluDOGs, especially in the context of the major-merger scenario for the quasar evolution, we compare the SMBH accretion of the four BluDOGs with other AGN populations. Figure 11 presents a diagram of $L_{\rm bol}$ versus the SMBH mass. As in Section 4.2, SDSS quasars (Shen et al. 2011) and WISSH quasars (Vietri et al. 2018) are used as comparison samples. For the SDSS quasars, we select only non-BAL quasars (`BAL < 1`) with the uncertainty of $L_{\rm bol}$ and $M_{\rm BH}$ less than 0.5 dex (`e_logBHCV < 0.5&e_logLbol < 0.5`), and adopt the C IV-based SMBH mass for a fair comparison with those of the BluDOGs. We also plot samples of 28 ERQs (Perrotta et al. 2019), five Hot DOGs (Wu et al. 2018), two power-law DOGs (Melbourne et al. 2011), and one Compton-thick (CT) DOG (Toba et al. 2020). Hot DOGs are DOGs with a special color of WISE (very faint in the 3.4 and 4.5 μm bands, but bright in the longer bands; Eisenhardt et al. 2012; Wu et al. 2012), while power-law DOGs are DOGs with a featureless power-law SED from the optical to MIR (e.g., Dey et al. 2008; Bussmann et al. 2012; Toba et al. 2015; Noboriguchi et al. 2019). The CT DOG was identified by the Nuclear Spectroscopic Telescope Array (Harrison et al. 2013) from the SDSS-WISE DOG sample. All but the CT DOGs have spectroscopic redshifts. The SMBH masses of the ERQs and the WISSH quasars are estimated from Hβ, while those of the Hot DOGs and the DOGs are estimated from Hα. The SMBH mass of the CT DOG was estimated by Toba et al. (2020) from the stellar mass by using an empirical relation between the stellar mass and SMBH mass (Kormendy & Ho 2013). Since Perrotta et al. (2019) and Melbourne et al. (2011) did not correct the absorption of dust, the $M_{\rm BH}$ of ERQs and DOGs are lower limits.

Figure 11 shows that the four BluDOGs are more luminous than the other AGN populations at a given SMBH mass, or equivalently, they have lower-mass SMBHs than the other AGN populations at a given bolometric luminosity. This suggests that the SMBH growth in the BluDOGs is more rapid than AGNs in comparison samples. Indeed, the Eddington ratios ($\lambda_{\rm Edd}$) of J0907, J1202, J1207, and J1443 are 1.10 ± 0.20, 3.89 ± 0.78, 2.19 ± 0.44, and 1.40 ± 0.23, respectively (Table 9), with the average value of 2.26. In other words, the SMBHs in the BluDOGs are now in the stage of the Eddington-limit or super-Eddington accretion. Even if the intrinsic SMBH masses are lower than those estimated (Section 3.4), the conclusion of this study remains qualitatively unchanged. The higher Eddington ratios compared to other populations suggest that the SMBHs in BluDOGs are in the most rapidly evolving phase during the entire evolutionary history of SMBHs. In the gas-rich major-merger scenario of Hopkins et al. (2008), the peak of the AGN activity (i.e., the mass growth of SMBHs)

corresponds to the transition phase from the optically thick to optically thin quasars, where the surrounding dust is blown out by the powerful AGN activity. Note that optically thick quasars in the major-merger scenario should be recognized as type 2 quasars in optical (the BLR cannot be observed due to the heavy dust reddening). Since optically thick quasars in the final stage of the evolution can be recognized as both type 1 and type 2, due to the orientation effect toward the dusty torus, the observed type 1 nature suggests the object is not in the early (optically thick) stage in the major-merger evolutionary scenario. Preferentially in AGNs with high $\lambda_{\rm Edd}$, a blue-wing feature tends to be observed (e.g., Aoki et al. 2005; Komossa et al. 2008). The observed characteristics of the BluDOGs such as the type 1 nature and the blue-wing feature of the C IV velocity profile are consistent with the picture that BluDOGs are in such a peak stage of the SMBH evolution.

To discuss the evolutionary relation among populations of dusty galaxies (BluDOGs, core ERQs, and Hot DOGs), we focus on $E(B-V)$ and kt_{80}. $E(B-V)$ for BluDOGs, core ERQs (Hamann et al. 2017), and Hot DOGs (Wu et al. 2018) are 0.273 ± 0.049, 0.242 ± 0.127, and 4.781 ± 1.986, respectively. The $E(B-V)$ of the Hot DOGs is significantly larger than that of the BluDOG and core ERQ samples, suggesting the Hot DOGs are thought to be in a heavily obscured phase. Since the kt_{80} of BluDOGs is smaller than that of core ERQs (Section 4.1), and the kt_{80} of MIR-detected quasars is close to that of BluDOGs (Figure 1 of Monadi & Bird 2022), the BluDOG phase is thought to be close to the optically thin quasar phase. Therefore, it is suggested that the evolutionary path of various AGN populations is "Hot DOGs—core ERQs—BluDOGs—optically thin quasars."

For AGNs in general, the mass accretion efficiency (η) is defined as the following:

$$\eta = \frac{L_{\rm bol}}{\dot{M}c^2}, \tag{4}$$

where $\dot{M}$ is the mass accretion rate. By multiplying the $\dot{M}$ and lifetime of BluDOGs ($t_{\rm life}$), we can roughly estimate the accreted mass ($M_{\rm acc}$) in the BluDOG phase. Bian & Zhao (2003) estimated $\log\eta = -1.61$ of Seyfert 1 galaxies and Palomar–Green quasars by assuming that the geometrically thin and optically thick standard α-prescription accretion disk model (Shakura & Sunyaev 1973). By assuming $\log\eta = -1.61$ and $t_{\rm life} = 1$ Myr (Noboriguchi et al. 2019), the estimated $M_{\rm acc}$ of J0907, J1202, J1207, and J1443 are about 1.68×10^7, 1.68×10^8, 2.19×10^7, and $6.93 \times 10^7\,M_\odot$. The SMBH masses reached when the SMBH masses of the BluDOGs are increased by the observed mass accretion rate during the typical lifetime of BluDOGs ($M_{\rm BH}^{+} = M_{\rm BH} + M_{\rm acc}$) of J0907, J1202, J1207, and J1443 are 1.86×10^8, 6.63×10^8, 1.32×10^8, and $6.17 \times 10^8\,M_\odot$, respectively. Therefore, the SMBH mass of BluDOGs increases by ~20% during the short BluDOG phase, suggesting that BluDOGs are actually in a rapidly glowing phase.

Figure 12 shows the Eddington ratios of various populations of AGNs as a function of redshift. The excess of $\lambda_{\rm Edd}$ of the four BluDOGs is more significant than the scatter of the $\lambda_{\rm Edd}$ distribution, suggesting that BluDOGs are a special class of AGNs that harbor SMBHs in the most actively evolving phase. Then, why is such a class of AGNs only found in a limited redshift range, $2.2 < z_{\rm sp} < 3.3$? A possible reason comes from

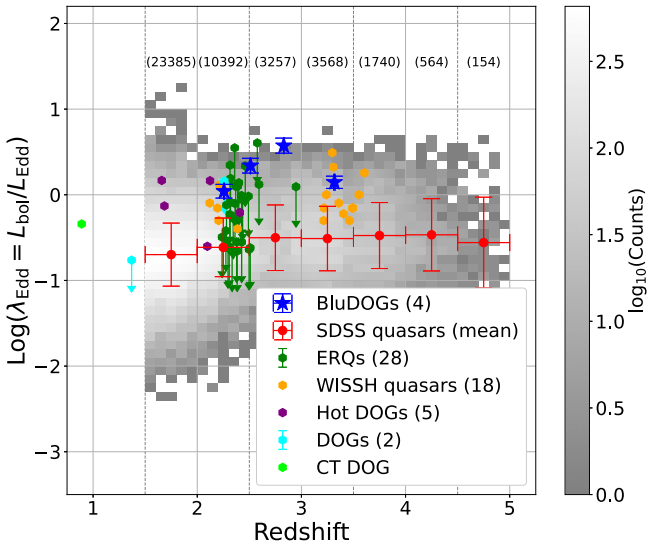

Figure 12. Diagram of the redshift vs. the Eddington ratio. The filled-blue stars and hexagons are the same as in Figure 11. The gray 2D histogram represents the number density of SDSS quasars (Shen et al. 2011). The red plots show the mean and standard deviation of $\lambda_{\rm Edd}$ in redshift bins with a width of $\Delta z = 0.5$. The numbers shown at the upper part denote the numbers of SDSS quasars in the redshift bins.

their selection criteria, as briefly mentioned in Section 4.1. Since the BluDOGs are selected by the blue excesses, which are largely caused by the contribution of strong BLR emission lines, the resultant redshift distribution would be biased such that the blue bands contain strong emission lines. It is also not clear whether the entire population of DOGs has systematically larger $\lambda_{\rm Edd}$ than ordinary type 1 quasars, due to the paucity of spectroscopic data. In order to reveal the total picture of the dust-enshrouded evolution of SMBHs, more systematic spectroscopic observations for various populations of BluDOGs and DOGs are needed.

5. Conclusion

We carried out spectroscopic observations of the four BluDOGs selected by Noboriguchi et al. (2019) using Subaru/FOCAS and VLT/FORS2. The analysis of the obtained spectroscopic data revealed the following spectroscopic properties of BluDOGs:

1. The rest-frame UV spectra of the BluDOGs show broad ($\gtrsim$2000 km s^{-1}) emission lines. This suggests that the BLRs of the BluDOGs are not completely obscured, albeit the very dusty nature inferred from their optical-IR SED.
2. The C IV lines of the BluDOGs show a significant blue wing, which is more prominent than in ordinary SDSS type 1 quasars. This suggests a presence of powerful nuclear outflow at the spatial scale of the BLR in the BluDOGs.
3. The REWs of their BLR lines are very large, REW (C IV) ~ 160 Å, ~7 times larger than the average of SDSS type 1 quasars. Such strong lines cause the flux excess of the two BluDOGs in the HSC g and r bands, while blue continuum emission also contributes the blue excess in the remaining two objects. The large REWs are not explained by the Baldwin effect. A possible origin is a powerful nuclear outflow in the BluDOGs causing a

selective obscuration of the nuclear region, as suggested for ERQs.

4. The Eddington ratios of the BluDOGs are higher than 1.0 and are systematically larger than other AGN populations. The mass accretion onto the SMBH in BluDOGs is in the mode of the Eddington limit or super-Eddington accretion.

All of the above results support the scenario that BluDOGs represent a population of AGNs in the transition phase from optically thick to optically thin quasars, i.e., in the blowing-out phase of the major-merger scenario for the evolution of an SMBH. The spectroscopic properties of the BluDOGs are similar to those of ERQs. For further understanding of the complete picture, more systematic spectroscopic observations are crucial, not only of BluDOGs but also of the whole population of DOGs.

The authors gratefully acknowledge the anonymous referee for a careful reading of the manuscript and very helpful comments. This study is based on data collected at the Subaru Telescope, which is operated by the National Astronomical Observatory of Japan, and observations collected at the European Southern Observatory under ESO program 0102.B-0614(A). We are honored and grateful for the opportunity to observe the universe from Mauna Kea, which has cultural, historical, and natural significance in Hawaii. The Hyper Suprime-Cam (HSC) Collaboration includes the astronomical communities of Japan, Taiwan, and Princeton University. The HSC instrumentation and software were developed by the National Astronomical Observatory of Japan (NAOJ), the Kavli Institute for the Physics and Mathematics of the Universe (Kavli IPMU), the University of Tokyo, the High Energy Accelerator Research Organization (KEK), the Academia Sinica Institute for Astronomy and Astrophysics in Taiwan (ASIAA), and Princeton University. Funding was contributed by the FIRST program from the Japanese Cabinet Office, the Ministry of Education, Culture, Sports, Science and Technology (MEXT), the Japan Society for the Promotion of Science (JSPS), Japan Science and Technology Agency (JST), the Toray Science Foundation, NAOJ, Kavli IPMU, KEK, ASIAA, and Princeton University. This paper makes use of software developed for the Large Synoptic Survey Telescope. We thank the LSST Project for making their code available as free software at http://dm.lsstcorp.org. The Pan-STARRS1 Surveys (PS1) have been made possible through contributions of the Institute for Astronomy, the University of Hawaii, the Pan-STARRS Project Office, the Max Planck Society and its participating institutes, the Max Planck Institute for Astronomy, Heidelberg and the Max Planck Institute for Extraterrestrial Physics, Garching, The Johns Hopkins University, Durham University, the University of Edinburgh, Queen's University Belfast, the Harvard-Smithsonian Center for Astrophysics, the Las Cumbres Observatory Global Telescope Network Incorporated, the National Central University of Taiwan, the Space Telescope Science Institute, the National Aeronautics and Space Administration under grant No. NNX08AR22G issued through the Planetary Science Division of the NASA Science Mission Directorate, the National Science Foundation under grant No. AST-1238877, the University of Maryland, and Eotvos Lorand University (ELTE) This publication has made use of data from the VIKING survey from VISTA at the ESO Paranal Observatory, program ID 179. A-2004. Data processing has been contributed by the VISTA Data Flow System at CASU, Cambridge and WFAU, Edinburgh. This publication makes use of data products from the Wide-field Infrared Survey Explorer, which is a joint project of the University of California, Los Angeles, and the Jet Propulsion Laboratory/California Institute of Technology, funded by the National Aeronautics and Space Administration. Herschel is an ESA space observatory with science instruments provided by European-led Principal Investigator consortia and with important participation from NASA. This research made use of Astropy,[22] a community-developed core Python package for Astronomy (Astropy Collaboration et al. 2013, 2018). We would like to thank Enago (www.enago.jp) for the English language review and Kohei Iwashita for helpful discussion. This study was financially supported by the Japan Society for the Promotion of Science (JSPS) KAKENHI grant Nos. 19J10458, 21H01126 (A.N.), 16H03958, 17H01114, 19H00697, 20H01949 (T.N.), 18J01050, 19K14759, 22H01266 (Y. Toba), 20H01939 (K.I.), and 20K04014 (Y. Terashima).

Software: Astropy, Astro-SCRAPPY, X-CIGALE, NumPy, Scipy.optimize.curve_fit, Recipe flexible execution workbench (Reflex).

Facilities: Subaru (FOCAS, HSC), VLT (FORS2), VISTA, WISE, and Herschel (PACS, SPIRE).

ORCID iDs

Akatoki Noboriguchi https://orcid.org/0000-0002-5197-8944
Tohru Nagao https://orcid.org/0000-0002-7402-5441
Yoshiki Toba https://orcid.org/0000-0002-3531-7863
Kohei Ichikawa https://orcid.org/0000-0002-4377-903X
Masaru Kajisawa https://orcid.org/0000-0002-1732-6387
Toshihiro Kawaguchi https://orcid.org/0000-0002-3866-9645
Yoshiki Matsuoka https://orcid.org/0000-0001-5063-0340
Kyoko Onishi https://orcid.org/0000-0002-0997-1060
Masafusa Onoue https://orcid.org/0000-0003-2984-6803
Koki Terao https://orcid.org/0000-0001-5899-9185
Yuichi Terashima https://orcid.org/0000-0003-1780-5481
Yoshihiro Ueda https://orcid.org/0000-0001-7821-6715
Takuji Yamashita https://orcid.org/0000-0002-4999-9965

References

Aihara, H., Arimoto, N., Armstrong, R., et al. 2018, PASJ, 70, S4
Aoki, K., Kawaguchi, T., & Ohta, K. 2005, ApJ, 618, 601
Appenzeller, I., Fricke, K., Fürtig, W., et al. 1998, Msngr, 94, 1
Arnaboldi, M., Neeser, M. J., Parker, L. C., et al. 2007, Msngr, 127, 28
Astropy Collaboration, Price-Whelan, A. M., Sipőcz, B. M., et al. 2018, AJ, 156, 123
Astropy Collaboration, Robitaille, T. P., Tollerud, E. J., et al. 2013, A&A, 558, A33
Baldwin, J. A. 1977, ApJ, 214, 679
Baskin, A., & Laor, A. 2004, MNRAS, 350, L31
Baskin, A., & Laor, A. 2005, MNRAS, 356, 1029
Bian, W.-H., & Zhao, Y.-H. 2003, PASJ, 55, 599
Bischetti, M., Piconcelli, E., Vietri, G., et al. 2017, A&A, 598, A122
Boquien, M., Burgarella, D., Roehlly, Y., et al. 2019, A&A, 622, A103
Bourne, N., Dunne, L., Maddox, S. J., et al. 2016, MNRAS, 462, 1714
Bruzual, G., & Charlot, S. 2003, MNRAS, 344, 1000
Burgarella, D., Buat, V., & Iglesias-Páramo, J. 2005, MNRAS, 360, 1413
Bussmann, R. S., Dey, A., Armus, L., et al. 2012, ApJ, 744, 150
Bussmann, R. S., Dey, A., Borys, C., et al. 2009, ApJ, 705, 184
Bussmann, R. S., Dey, A., Lotz, J., et al. 2011, ApJ, 733, 21

[22] http://www.astropy.org

Calzetti, D., Armus, L., Bohlin, R. C., et al. 2000, ApJ, 533, 682
Cardelli, J. A., Clayton, G. C., & Mathis, J. S. 1989, ApJ, 345, 245
Chabrier, G. 2003, PASP, 115, 763
Ciesla, L., Charmandaris, V., Georgakakis, A., et al. 2015, A&A, 576, A10
Coatman, L., Hewett, P. C., Banerji, M., et al. 2017, MNRAS, 465, 2120
Collin, S., Kawaguchi, T., Peterson, B. M., & Vestergaard, M. 2006, A&A, 456, 75
Croom, S. M., Rhook, K., Corbett, E. A., et al. 2002, MNRAS, 337, 275
Cutri, R. M. 2014, VizieR On-line Data Catalog: II/328
Dale, D. A., Helou, G., Magdis, G. E., et al. 2014, ApJ, 784, 83
Dawson, K. S., Schlegel, D. J., Ahn, C. P., et al. 2013, AJ, 145, 10
De Robertis, M. 1985, ApJ, 289, 67
Denney, K. D., Peterson, B. M., Pogge, R. W., et al. 2009, ApJL, 704, L80
Desai, V., Soifer, B. T., Dey, A., et al. 2009, ApJ, 700, 1190
Dey, A., Soifer, B. T., Desai, V., et al. 2008, ApJ, 677, 943
Dietrich, M., Hamann, F., Shields, J. C., et al. 2002, ApJ, 581, 912
Ding, X., Silverman, J., Treu, T., et al. 2020, ApJ, 888, 37
Eales, S., Dunne, L., Clements, D., et al. 2010, PASP, 122, 499
Eisenhardt, P. R. M., Wu, J., Tsai, C.-W., et al. 2012, ApJ, 755, 173
Eisenstein, D. J., Weinberg, D. H., Agol, E., et al. 2011, AJ, 142, 72
Feibelman, W. A. 1983, A&A, 122, 335
Ferrarese, L., & Merritt, D. 2000, ApJL, 539, L9
Fiore, F., Grazian, A., Santini, P., et al. 2008, ApJ, 672, 94
Freudling, W., Romaniello, M., Bramich, D. M., et al. 2013, A&A, 559, A96
Gebhardt, K., Bender, R., Bower, G., et al. 2000, ApJL, 539, L13
Goulding, A. D., Greene, J. E., Bezanson, R., et al. 2018, PASJ, 70, S37
Griffin, M. J., Abergel, A., Abreu, A., et al. 2010, A&A, 518, L3
Hamann, F., Zakamska, N. L., Ross, N., et al. 2017, MNRAS, 464, 3431
Harrison, F. A., Craig, W. W., Christensen, F. E., et al. 2013, ApJ, 770, 103
Hopkins, P. F., Hernquist, L., Cox, T. J., & Kereš, D. 2008, ApJS, 175, 356
Horne, K., Peterson, B. M., Collier, S. J., & Netzer, H. 2004, PASP, 116, 465
Inoue, A. K. 2011, MNRAS, 415, 2920
Kashikawa, N., Aoki, K., Asai, R., et al. 2002, PASJ, 54, 819
Kawanomoto, S., Uraguchi, F., Komiyama, Y., et al. 2018, PASJ, 70, 66
Kinney, A. L., Rivolo, A. R., & Koratkar, A. P. 1990, ApJ, 357, 338
Kollatschny, W., Ulbrich, K., Zetzl, M., Kaspi, S., & Haas, M. 2014, A&A, 566, A106
Komossa, S., Xu, D., Zhou, H., Storchi-Bergmann, T., & Binette, L. 2008, ApJ, 680, 926
Kormendy, J., & Ho, L. C. 2013, ARA&A, 51, 511
Leitherer, C., Li, I. H., Calzetti, D., & Heckman, T. M. 2002, ApJS, 140, 303
Li, Y.-R., Wang, J.-M., Ho, L. C., Du, P., & Bai, J.-M. 2013, ApJ, 779, 110
Magorrian, J., Tremaine, S., Richstone, D., et al. 1998, AJ, 115, 2285
Marconi, A., & Hunt, L. K. 2003, ApJL, 589, L21
McCully, C., & Tewes, M. 2019, Astro-SCRAPPY: Speedy Cosmic Ray Annihilation Package in Python, Astrophysics Source Code Library, ascl:1907.032
Melbourne, J., Peng, C. Y., Soifer, B. T., et al. 2011, AJ, 141, 141
Melbourne, J., Soifer, B. T., Desai, V., et al. 2012, AJ, 143, 125
Miyazaki, S., Komiyama, Y., Kawanomoto, S., et al. 2018, PASJ, 70, S1
Monadi, R., & Bird, S. 2022, MNRAS, 511, 3501
Moran, E. C., Halpern, J. P., & Helfand, D. J. 1996, ApJS, 106, 341
Netzer, H. 2015, ARA&A, 53, 365
Niida, M., Nagao, T., Ikeda, H., et al. 2016, ApJ, 832, 208
Noboriguchi, A., Nagao, T., Toba, Y., et al. 2019, ApJ, 876, 132
Noll, S., Burgarella, D., Giovannoli, E., et al. 2009, A&A, 507, 1793
Pancoast, A., Brewer, B. J., Treu, T., et al. 2014, MNRAS, 445, 3073
Perrotta, S., Hamann, F., Zakamska, N. L., et al. 2019, MNRAS, 488, 4126
Pilbratt, G. L., Riedinger, J. R., Passvogel, T., et al. 2010, A&A, 518, L1
Poglitsch, A., Waelkens, C., Geis, N., et al. 2010, A&A, 518, L2
Pope, A., Bussmann, R. S., Dey, A., et al. 2008, ApJ, 689, 127
Ross, N. P., Hamann, F., Zakamska, N. L., et al. 2015, MNRAS, 453, 3932
Sanders, D. B., Soifer, B. T., Elias, J. H., et al. 1988, ApJ, 325, 74
Schlegel, D. J., Finkbeiner, D. P., & Davis, M. 1998, ApJ, 500, 525
Shakura, N. I., & Sunyaev, R. A. 1973, A&A, 500, 33
Shen, Y. 2013, BASI, 41, 61
Shen, Y., Richards, G. T., Strauss, M. A., et al. 2011, ApJS, 194, 45
Stalevski, M., Ricci, C., Ueda, Y., et al. 2016, MNRAS, 458, 2288
Toba, Y., Bae, H.-J., Nagao, T., et al. 2017a, ApJ, 850, 140
Toba, Y., & Nagao, T. 2016, ApJ, 820, 46
Toba, Y., Nagao, T., Kajisawa, M., et al. 2017b, ApJ, 835, 36
Toba, Y., Nagao, T., Strauss, M. A., et al. 2015, PASJ, 67, 86
Toba, Y., Yamashita, T., Nagao, T., et al. 2019, ApJS, 243, 15
Toba, Y., Yamada, S., Ueda, Y., et al. 2020, ApJ, 888, 8
Toba, Y., Liu, T., Urrutia, T., et al. 2022, A&A, 661, A15
Treister, E., Schawinski, K., Urry, C. M., & Simmons, B. D. 2012, ApJL, 758, L39
Tremaine, S., Gebhardt, K., Bender, R., et al. 2002, ApJ, 574, 740
Valiante, E., Smith, M. W. L., Eales, S., et al. 2016, MNRAS, 462, 3146
van Dokkum, P. G. 2001, PASP, 113, 1420
Vanden Berk, D. E., Richards, G. T., Bauer, A., et al. 2001, AJ, 122, 549
Véron-Cetty, M. P., Véron, P., & Gonçalves, A. C. 2001, A&A, 372, 730
Vestergaard, M., & Osmer, P. S. 2009, ApJ, 699, 800
Vestergaard, M., & Peterson, B. M. 2006, ApJ, 641, 689
Vietri, G., Piconcelli, E., Bischetti, M., et al. 2018, A&A, 617, A81
Villar Martín, M., Perna, M., Humphrey, A., et al. 2020, A&A, 634, A116
Wright, E. L., Eisenhardt, P. R. M., Mainzer, A. K., et al. 2010, AJ, 140, 1868
Wu, J., Jun, H. D., Assef, R. J., et al. 2018, ApJ, 852, 96
Wu, J., Tsai, C.-W., Sayers, J., et al. 2012, ApJ, 756, 96
Yang, G., Boquien, M., Buat, V., et al. 2020, MNRAS, 491, 740
York, D. G., Adelman, J., Anderson, J. E., Jr., et al. 2000, AJ, 120, 1579
Zamfir, S., Sulentic, J. W., Marziani, P., & Dultzin, D. 2010, MNRAS, 403, 1759
Zou, F., Brandt, W. N., Vito, F., et al. 2020, MNRAS, 499, 1823